REPORT DOCUMENTATION PAGE

The public reporting burden for this collection of information is estimated to average 1 hour per response, including the time for reviewing instructions, searching existing data sources, gathering and maintaining the data needed, and completing and reviewing the collection of information. Send comments regarding this burden estimate or any other aspect of this collection of information, including suggestions for reducing the burden, to the Department of Defense, Executive Service Directorate (0704-0188). Respondents should be aware that notwithstanding any other provision of law, no person shall be subject to any penalty for failing to comply with a collection of information if it does not display a currently valid OMB control number.

PLEASE DO NOT RETURN YOUR FORM TO THE ABOVE ORGANIZATION.

1. REPORT DATE *(DD-MM-YYYY)*	2. REPORT TYPE	3. DATES COVERED *(From - To)*
01-6-2012	Master's Thesis	JAN 2012 - JUN 2012

4. TITLE AND SUBTITLE
Remote Nondestructive Evaluation of Composite-Steel Interface by Acoustic Laser Vibrometry

5a. CONTRACT NUMBER
N00244-09-G-0014

5b. GRANT NUMBER

5c. PROGRAM ELEMENT NUMBER

6. AUTHOR(S)
Timothy James Emge II

5d. PROJECT NUMBER

5e. TASK NUMBER

5f. WORK UNIT NUMBER

7. PERFORMING ORGANIZATION NAME(S) AND ADDRESS(ES)
Massachusetts Institute of Technology

8. PERFORMING ORGANIZATION REPORT NUMBER

9. SPONSORING/MONITORING AGENCY NAME(S) AND ADDRESS(ES)
Naval Postgraduate School
Monterey, CA 93943

10. SPONSOR/MONITOR'S ACRONYM(S)
NPS

11. SPONSOR/MONITOR'S REPORT NUMBER(S)

12. DISTRIBUTION/AVAILABILITY STATEMENT
1. DISTRIBUTION STATEMENT A. Approved for public release; distribution is unlimited.

13. SUPPLEMENTARY NOTES

14. ABSTRACT
Composite materials are increasingly being used in both civil and ship structures. In particular, fiber reinforced polymer (FRP) composites are being utilized. FRP materials are most often employed to reinforce aging or damaged portions of civil structures. On naval vessels, FRP materials are incorporated to reduce weight, particularly up high, and to reduce radar cross section, thereby increasing stealth capability. In both cases of FRP use, it is usually in conjunction with some other material, oftentimes steel. It is beneficial when using FRP and steel to adhesively bond them together. When these materials are joined adhesively, the most common failure mode is debonding or delamination at the interface of the adhesive with the steel and composite materials. These defects are often difficult to discern without the aid of some form of nondestructive testing (NDT).

15. SUBJECT TERMS

16. SECURITY CLASSIFICATION OF:			17. LIMITATION OF ABSTRACT	18. NUMBER OF PAGES	19a. NAME OF RESPONSIBLE PERSON
a. REPORT	b. ABSTRACT	c. THIS PAGE	UU	99	Julie Zack
					19b. TELEPHONE NUMBER *(Include area code)* (831) 656-2319

Reset

Remote Nondestructive Evaluation of Composite-Steel Interface by Acoustic Laser Vibrometry

by

Timothy James Emge II

Bachelor of Science in Ocean Engineering
United States Naval Academy, 2007

Submitted to the Department of Mechanical Engineering and the Department of Civil and Environmental Engineering in Partial Fulfillment of the Requirements for the Degrees of

Naval Engineer

and

Master of Science in Civil and Environmental Engineering

at the
Massachusetts Institute of Technology
June 2012
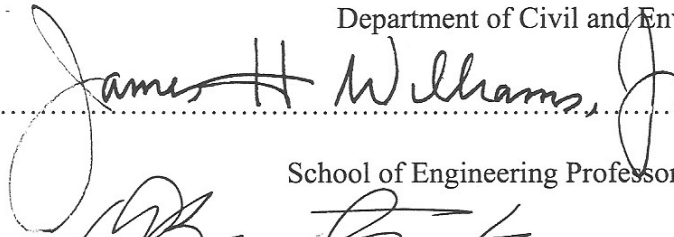
Signature of Author ....
Department of Mechanical Engineering
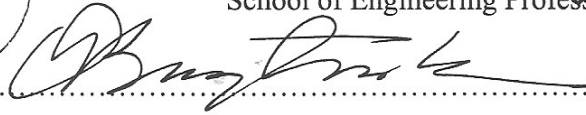Department of Civil and Environmental Engineering
May 11, 2012

Certified by ....
James H. Williams, Jr.
School of Engineering Professor of Teaching Excellence
Thesis Reader
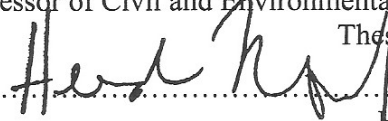
Certified by ....
Oral Büyüköztürk
Professor of Civil and Environmental Engineering
Thesis Supervisor

Accepted by ....
Heidi M. Nepf
Chair, Departmental Committee for Graduate Students

Accepted by ....
David E. Hardt
Ralph E. and Eloise F. Cross Professor of Mechanical Engineering
Chair, Departmental Committee on Graduate Students

Remote Nondestructive Evaluation of Composite-Steel Interface by Acoustic Laser Vibrometry

by

Timothy James Emge II

Submitted to the Department of Mechanical Engineering and the Department of Civil and Environmental Engineering on May 11, 2012 in Partial Fulfillment of the Requirements for the Degrees of Naval Engineer and Master of Science in Civil and Environmental Engineering

Abstract

Composite materials are increasingly being used in both civil and ship structures. In particular, fiber reinforced polymer (FRP) composites are being utilized. FRP materials are most often employed to reinforce aging or damaged portions of civil structures. On naval vessels, FRP materials are incorporated to reduce weight, particularly up high, and to reduce radar cross section, thereby increasing stealth capability. In both cases of FRP use, it is usually in conjunction with some other material, oftentimes steel. It is beneficial when using FRP and steel to adhesively bond them together. When these materials are joined adhesively, the most common failure mode is debonding or delamination at the interface of the adhesive with the steel and composite materials. These defects are often difficult to discern without the aid of some form of nondestructive testing (NDT).

Acoustic laser vibrometry is a relatively new method of NDT that shows a lot of promise in analysis of this interface. In this approach, an airborne acoustic wave is utilized to excite the location of the damage underneath the FRP sheets/plates and the target vibration is measured using a laser vibrometer. To study the acoustic laser method, a defect specimen was created from a plate of AL6XN stainless steel and a plate of glass FRP adhesively bonded on their faces with a purposely placed elliptical debonding defect. A number of parameters of the acoustic laser vibrometry system were varied and trends were found. Additionally, grid data was collected from the defect specimen and a defect mapping was created. Theoretical and finite element models were produced and compared to measured results. The close correlation of the results from these three methods validated them all.

Thesis Supervisor: Oral Buyukozturk
Titles: Professor of Civil and Environmental Engineering

Thesis Reader: James H. Williams, Jr.
Titles: School of Engineering Professor of Teaching Excellence, Charles F. Hopewell Faculty Fellow, Professor of Writing and Humanistic Studies

Acknowledgements

Throughout the course of my education at MIT there are a number of people without whom my completion of these degrees and this thesis would not have been possible.

First I would like to thank my thesis supervisor, Professor Oral Buyukozturk for his guidance and support throughout the thesis process. I would also like to thank my thesis reader, Professor James H. Williams, Jr. (who is supported by the DDG-1000 Program Manager/NAVSEA PMS 500 and the DDG-1000 Ship Design Manager/NAVSEA 05D) for his mentoring and support. In addition, Rob Haupt provided a valuable contribution to the thesis and supervised the experiments conducted at MIT Lincoln Laboratory, which supplied the laser vibrometry equipment and work space. Justin Chen was also of great assistance in the experimentation and data analysis portions of this research.

I would also like to thank Captain Mark Thomas, USN, Commander Pete Small, USN, and Captain Mark Welsh, USN (ret) for their mentoring and advice. Their contribution to my growth as a naval officer and engineer has been paramount.

Additionally I would like to thank the U.S. Navy for financial support and giving me the great opportunity to learn at one of the best institutions in the world.

I would like to thank my parents, Tim and Debbie Emge, and my brother, Andrew Emge, for their constant love and support of my endeavors.

Last, but certainly not least, I would like to express my deepest thanks to the love of my life, my wife, Jennifer. Her steadfast love and unceasing flexibility to our ever-changing adventure of life have made it possible for me to succeed.

Table of Contents

List of Figures

List of Tables

1 Background

Composite materials are made of two or more constituent materials with significantly different physical properties. The two materials are distinct in the finished composite product, however, the properties of the composite material are generally much different than either of the constituent materials. One type of composite that has seen significant use is the fiber reinforced polymer (FRP) which usually consists of a mesh of fibers with a matrix resin dispersed between the different layers of fibers. Most FRP materials have an extremely high strength to weight ratio which makes them ideal for any application where weight can become an issue. Currently, composites are mostly used in the aerospace field but have seen some use in the realms of ships and civil structures.

While it is prohibitively expensive to use composite FRP materials for the entire structure of a bridge or a large ship it is cost-effective to use them in conjunction with other materials like concrete and steel. Composite materials are currently used in structures to shore up steel and concrete members in order to increase the lifespan of the structures. They are also used for components of naval ship construction due to their high strength to weight ratio and also because the designer has the ability to tune the material to give the ship a smaller radar cross-section thereby enhancing its stealthiness.

1.1 FRP use in civil structures

FRP materials are being used on civil engineering structures to repair or increase the lifespan of older structures. The advantage of the composite material is its high stiffness to weight ratio which can significantly stiffen an older structure while having little impact on the structure's dead load. Examples of FRP use include wrapping concrete columns for better confinement or attaching to concrete and steel beams for increased bending capacity. The examples further discussed will specifically focus on the cases where FRP materials are bonded to steel or other metals as that is the focus of this research.

There are many structures (buildings or bridges) made with metals that require retrofitting or strengthening to meet the ever increasing load demands on the structure. The typical way to retrofit or repair an aging or damaged structure is to cut out and replace material or simply place additional plate over the area needing retrofit. There are many disadvantages to this type of repair including (Hollaway and Cadei 2002):

- The installation procedure is labor intensive and time consuming.

10

- It requires drilling and extensive lap-splicing requiring the heavy steel plates to remain in position until after fabrication.
- There is potential for weld fatigue cracking at the plate ends and distortion of the metallic system.
- The increase in weight of the members may lead to deficiency in member capacity and increased deflection.
- Drilling of existing structure causes a temporary weakening of the structure.

There are significant advantages to conducting retrofit with composite materials such as glass fiber reinforced polymer (GFRP) or carbon fiber reinforced polymer (CFRP). Some of these are as follows (Hollaway and Cadei 2002):

- FRP materials can be readily implemented in the field.
- There is no heavy support equipment required due to the light weight of the plates.
- FRPs have good durability characteristics.
- There is minimal disruption to normal operation of the structure.

FRP can be used to retrofit a variety of metals, most commonly cast iron, wrought iron, and steel. The use of FRP materials for metal structure retrofit has been more common in the United Kingdom than anywhere else in the world. Some examples of structures that have been successfully retrofitted are given below.

The King Street Railway Bridge in Mold, North Wales, United Kingdom was constructed in 1870 from cast iron. The free span of the bridge is 8.93 m (29.30 ft) but due to age, and decreased load carrying capacity, the structure had to be propped up at midspan until a strengthening plan could be devised. Even with the propped span, a weight restriction of 17 metric tons (18.7 short tons) was applied to the bridge, well below the desired capacity of 40 metric tons (44 short tons). The strengthening plan required the use of CFRP plates to stiffen the longitudinal cast iron girders running the length of the span as shown in Figure 1. The composite plates were also outfitted with strain gauges to monitor the performance of the structural system after strengthening. Structural monitoring under known loads has shown the strengthening with CFRP has achieved the desired results (Farmer and Smith 2001).

Figure 1: King Street Railway bridge with CFRP plates installed on cast iron girders with strain gauges for structural health monitoring (Farmer and Smith 2001)

Another example of the use of FRP material for bridge retrofit was conducted on a bridge on Interstate 95 in Newark, Delaware. In this case the retrofit was not conducted on an aging, deteriorated structure, but on a structure in good condition so that failure of the FRP system would not compromise the integrity of the structure as a whole. The bridge consists of three spans totaling 35 m (114.8 ft) and the portion chosen to implement CFRP strengthening was a single steel girder in one of the 7.5 m (24.6 ft) approach spans. Figure 2 shows the CFRP plates installed beneath the girder during the adhesive curing process. The strain in the girder after strengthening was compared to pre installation measured strains under the same load. The CFRP strengthening increased the global flexural stiffness of the girder by 11.6%. Figure 3 shows the pre and post retrofit strain in the girder chosen for installation. This increased stiffness shown on a bridge in good condition is promising for the use of composite stiffening of deteriorated steel structures (Miller, et al. 2001).
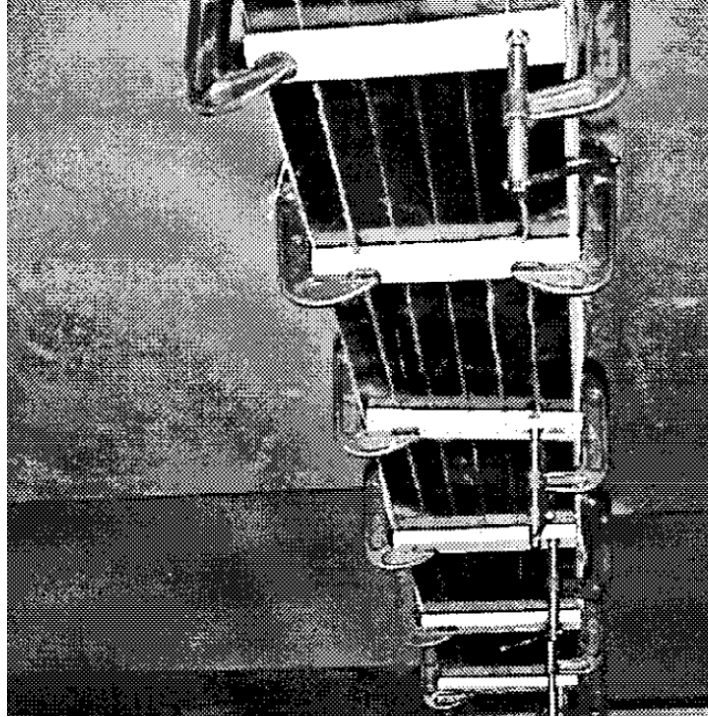
Figure 2: CFRP plates installed on Interstate 95 bridge in Newark, Delaware. Clamped during the curing process (Miller, et al. 2001)
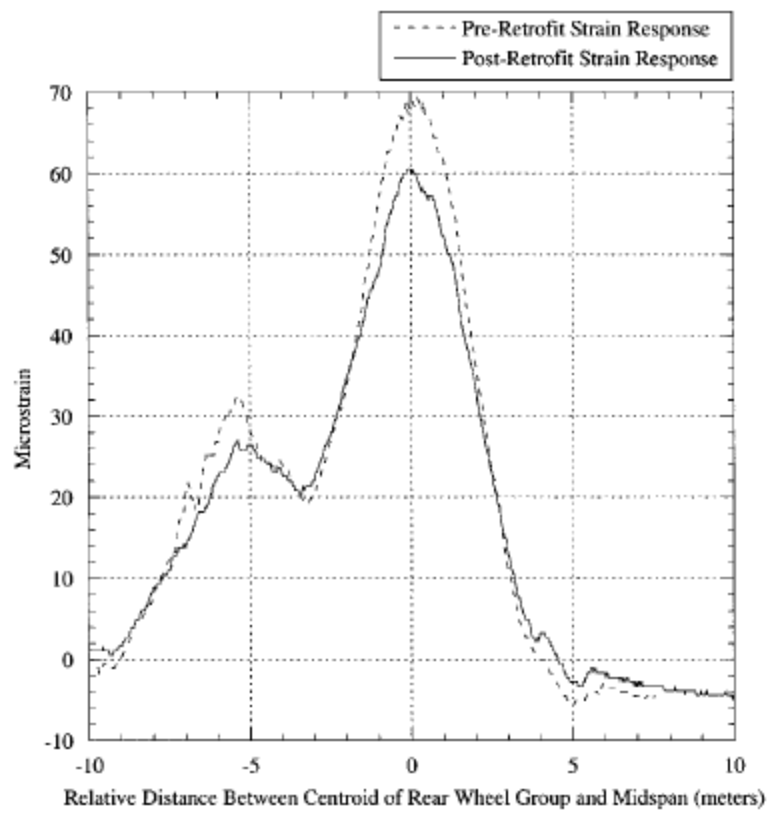
Figure 3: Pre- and post-retrofit strain response of Interstate 95 bridge in Newark, Delaware (Miller, et al. 2001)

The Slattocks Canal Bridge in Rochdale, United Kingdom was built in 1936 with steel girders supporting a reinforced concrete deck. The girders have a free span of 7.62 m (25 ft) between abutments. Due to deterioration the bridge's load was limited to 17 metric tons (18.7 short tons), but its desired load was to be 40 metric tons (44 short tons). CFRP plates were chosen to retrofit the structure due to minimal impact to traffic carried by the bridge and minimal impact to the clearance below the bridge. The plates used were only 10 mm (0.39 in) thick which did not affect the clearance above the waterway below. As seen in Figure 4, the plates did not require a large amount of equipment for installation due to their light weight. After installation the bridge was able to have the load restriction removed and was able to carry loads up to 40 metric tons as designed. The limited impact to normal operation of the bridge made the use of CFRP strengthening less expensive than other retrofit options (Luke 2001).

Figure 4: Installation of CFRP plates on girders of Slattocks Canal Bridge in Rochdale, UK (Luke 2001)

1.2 FRP use in Naval Structures

The use of FRP materials in ships focuses on new construction rather than rehabilitation as in civil structures. There is potential to use them for repair with similar benefits as seen in civil structures, but there are additional reasons why using composite materials in new ship construction is beneficial. In particular composite use in ships is beneficial to naval ships due to their necessitated high performance and increased tolerance for additional cost. Some of the advantages of using composite materials over metals in ships are listed as follows:

- Increased stealth

14

- Lower total ownership cost

- Decreased weight

- Ability to design/build complex hull shapes with minimal cost and weight increase

To increase stealth, composite materials can be specifically "tuned" to absorb certain bands of the electro-magnetic spectrum therefore making the ship less susceptible to radar detection. Additionally composite materials can be made to high tolerances with minimal residual stresses thereby reducing dishing of plates as is seen in many metal ships. Dishing of multiple panels on naval ships (commonly referred to as hungry horse) leads to increased radar cross section due to numerous concave surfaces for electro-magnetic reflection. Composites can decrease total ownership cost when compared with other metals because they are less susceptible to corrosion and do not require anti-corrosion coatings. The decreased weight of a composite ship can lead to increased payload, higher top speed, greater range, and reduced fuel consumption. Due to the construction methods employed with composite materials, there is minimal difficulty in molding and constructing very complex hull shapes which is not true with steel or other metal construction (Barsoum 2003).

This all sounds great for the use of composites in ship construction, but there are a number of issues. One is that even though composites have a high strength to weight ratio they are not as strong as most steels and therefore cannot be used to construct vessels much greater than 60 m (200 ft) in length. Additionally, composites are very expensive. As of 2003 it was $12-18/lb for CFRP compared to $0.45/lb for carbon steel and $3/lb for stainless steel (Barsoum 2003). These reasons make it desirable to use composites for the construction of a portion of the ship rather than the entire ship for larger surface combatants commonly used by the U.S. Navy. Some examples of composite use in ship construction by both the U.S. and other foreign navies are given below.

The U.S. Navy's LPD-17 San Antonio class of amphibious transport dock ship is designed using two masts made of composite materials. This ship is 200 m (661 ft) long and displaces 22,680 metric tons (22,320 long tons), much too large to be constructed entirely out of composites. The composite masts are advanced enclosed mast/sensor (AEM/S) systems which incorporate a high quality fiberglass vinyl/ester skin with lightweight foam or balsa cores. The masts are approximately 24.4 m (80 ft) tall by 10.7 m (35 ft) in diameter. The AEM/S system was used in this case to maintain the required low radar cross section and to decrease lifecycle

15

maintenance (Camponeschi, et al. 2007). Figure 5 shows the AEM/S system as installed on the San Antonio class of ship with the circled areas indicating the two composite masts.
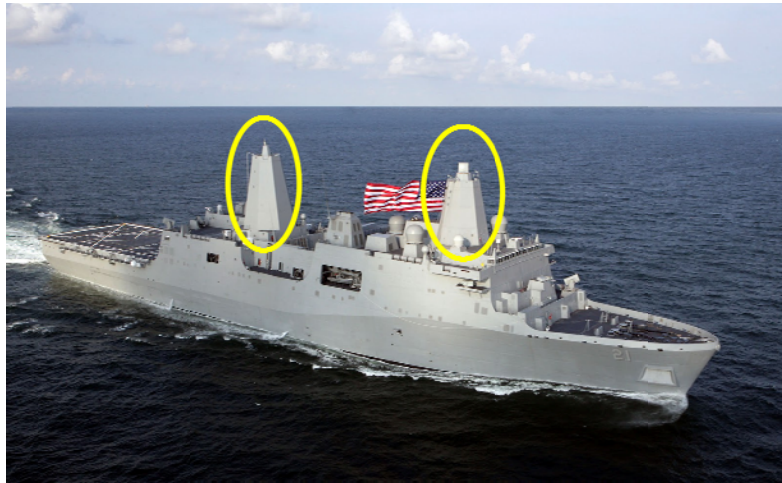
Figure 5: LPD-17 San Antonio class ship with composite masts circled (NavSource Naval History: Photographic History of the U.S. Navy 2009)

Another use of composites by the U.S. Navy is the DDG-1000 Zumwalt class guided missile destroyer. The Zumwalt is currently under construction and is to have a composite deckhouse/superstructure as shown by the circled portion in Figure 6. The deckhouse's first three levels are to be made of steel with the upper four levels to be made from balsa-cored carbon/vinyl ester sandwich panels. The ship is to be 180 m (600 ft) long with a displacement of 14,798 metric tons (14,564 long tons), again too large to be constructed entirely of composite materials. A large requirement of the DDG-1000 was a greatly reduced radar signature which necessitated the unique tumblehome hull form and large-scale use of composites. The composite portion of the superstructure is to be approximately 39.6 m (130 ft) long by 18.3 m (60 ft) wide by 12.2 m (40 ft) high (LeGault 2010). The design incorporates as many flat panels as possible to help decrease construction costs of the composite portion of the ship. The composite superstructure greatly decreases the radar cross section of the ship and reduces weight at height thereby making the ship more stable.
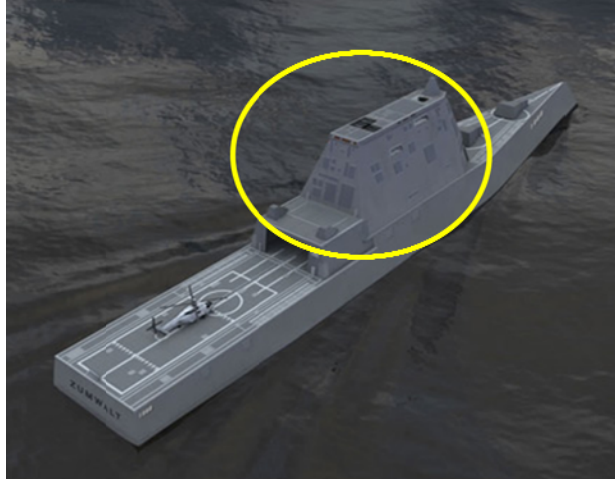
Figure 6: DDG-1000 with composite superstructure circled (DDG-1000 Zumwalt Class - Multimission Destroyer, United States of America 2011)

The Swedish Navy has used composites for the entire construction of its Visby class corvette. The Visby, which is 73 m (239.5 ft) long and displaces 600 metric tons (590 long tons), is constructed out of CFRP sandwich material. Stealth was a primary design requirement as such a small ship cannot take many hits from either missiles or surface gunfire. Therefore reduction of all ship signatures was used in this design to include optical and infrared signature, above water acoustic and hydroacoustic signature, underwater electrical potential and magnetic signature, pressure signature, radar cross section, and actively emitted signals (Visby Class, Sweden 2011). Its design uses a reduction of angles by maintaining a very flat surface as can be seen in Figure 7. This drastically decreases the radar cross section of the ship thereby making it stealthier. The use of composites led to a dramatic decrease in the ship's displacement which is half of a conventional corvette. This allows for a very high speed vessel as evidenced by the Visby's top speed of 64.8+ km/hr (35+ kts) (Summers 2004).

Figure 7: Swedish Visby class corvette built entirely of composite materials (Visby Class Corvette 2008)

17

1.3 Current Issues of FRP Use

One issue with the use of composites in conjunction with other materials is how to join the composite to the other material (Simler and Brown 2003). In some cases the composite can be made using a wet layup directly on the concrete or steel so long as the resin is compatible with the base structural material. Due to time constraints and the locations on structures where composites are typically applied this method is less than ideal. Another method is simply bolting the composite material to the steel or concrete. This is the simplest method but presents issues because it is time consuming usually requiring workers to tighten every bolt by hand and the bolt holes induce stress concentration areas in the structure. These stress concentration areas make it necessary to make the structure larger in the area of the bolts which in turn adds weight to the composite thereby detracting from its main advantage of being lightweight.

Another way to join the two materials is to use an adhesive to join the already completed composite to the steel or concrete. This method shows much promise as the stress concentration is less of an issue than bolting and it is much quicker than a wet layup on the base structure. Much work has already been completed in this area to help determine the best ways to adhere the two dissimilar components (specifically stainless steel/E-glass joints) (Wang and Gupta 2005). The stresses between the dissimilar components and the adhesive can be accurately calculated which leads to the determination of whether the adhesive will be able to withstand the loads it must carry (Williams 1975). However the issue with adhesively bonding the two materials is the difficulty determining if the joint has any flaws once in place. The possible failure modes for an adhesively joined steel-composite joint are as follows (Zhao and Zhang 2007):

- Steel/adhesive interface failure
- Adhesive layer failure (cohesive failure)
- FRP/adhesive interface failure
- FRP delamination
- FRP rupture
- Steel yielding

A majority of these failure modes deal with debonding phenomena as shown in Figure 8. Debonding presents a critical barrier to the use of FRP composites in conjunction with steel (Buyukozturk, Gunes and Erdem 2004). It is necessary to have a good understanding of the

18

status of FRP-steel joints in structures in order to accurately predict structure strength. Since many times the joint cannot be seen visually, the use of some form of non-destructive testing (NDT) is required.
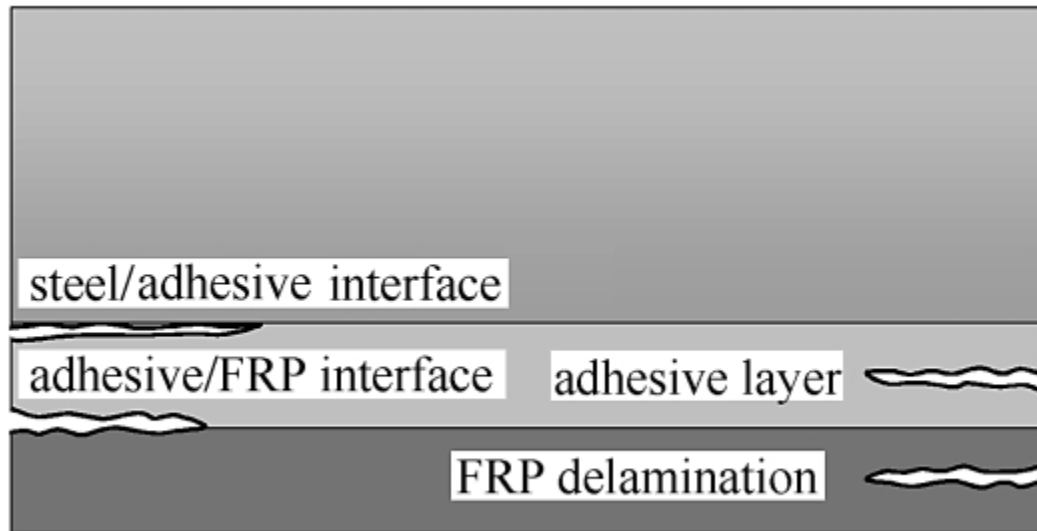
Figure 8: Various types of debonding occurring between adhesively bonded FRP and steel (Buyukozturk, Gunes and Erdem 2004)

1.4 Nondestructive Testing (NDT) Methods

There are many methods of NDT that can be used on composite joints with other materials. Methods such as stress wave (acoustic), infrared thermography, x-ray, and radar (microwave) have all seen use to varying levels of success. The issue is that all of these methods require direct contact with the material to be tested and sometimes require direct contact with both sides of the material. While this is not a huge issue for aerospace applications of composites where the components to be tested are relatively small, it can become impossible for naval and civil structures where the components are massive. The requirement to conduct NDT on materials on such large structures adds cost to the construction process and throughout the life of the structure. A stand-off method that does not require direct contact with the structure would allow for much more rapid NDT thereby greatly reducing the cost and time while still ensuring a safe joint between the composite and its base material.

To effectively detect and characterize damages in FRP structures a NDT technology that is capable of detecting (1) the extent of delamination in the interface region, (2) debonding of FRP-steel and FRP-FRP interface, (3) decohesion in epoxy or FRP constituent, and (4) sizeable

19

air pockets trapped in the vicinity of the interface region during manufacturing is necessary. Currently, several NDT technologies have been under investigation.

Acoustic methods are based upon elastic wave propagation in solids. They include pulse-echo, impact echo, ultrasonic, acoustic emission, and spectral analysis of surface waves (SASW) techniques. Disadvantages include the need of intimate contact between the equipment and the subject, the use of a sound couplant, as well as the existence of multiple paths through the same subject that make result interpretations difficult or erroneous (Liang, Sun and Ansari 2004) (Nagem, Seng and Williams 2000).

Infrared thermography is based on the detection of heat flow in the subject in which air gaps resulting from delamination act as insulators, which block out the proper heat flow. Data interpretation is, however, complicated because of varying ambient temperature conditions and surface emissivity variations, which is a function of surface properties. Additionally this method requires direct contact with the material to be tested (Krishnapillai, et al. 2005) (Williams and Nagem 1983).

Radiography-based evaluation methods use high frequency electromagnetic radiation (X-rays and Gamma rays) or particular beams (beta rays and neutron radiation) passing through the subject and exposing it onto a film on the other side of the subject. Limitations include the need to access both sides of the subject, the need of safety precautions, long exposure time, and only producing two-dimensional (2D) images of three-dimensional (3D) subjects (Nagem, Seng and Williams 2000).

Microwave or radar has been used extensively for site characterization in geotechnical engineering. It has also been used to evaluate concrete structures, pavements, and bridges (Fenning and Brown 1995) (Mellet 1995). Radar involves the generation and transmission of electromagnetic impulse into materials with different dielectric constants (Clemena 1991) (Buyukozturk and Rhim 1998). Voids, delaminations, and material characteristics can be detected and interpreted from the pulse reflections (Buyukozturk and Yu 2008). Issues with radar NDT include high noise levels, resolution and interpretation of measurements, and the inability to use with carbon fiber and metal components due to reflection.

The laser Doppler vibrometer (LDV) method has been studied to a limited extent for detecting delamination in composite specimens. The laser Doppler technique is based on Doppler shifts effect which characterizes the frequency changes owing to movement of the

20

source, receiver, propagation medium, or intervening reflector or scatter. It has been widely applied to the velocity determination in fluid mechanics by utilizing the optical beating or differential Doppler technique (Drain 1980). The velocity of target is calculated by the Doppler shift frequency, the wavelength of the laser (light), and the angle between the direction of illumination and the direction in which the scattered laser beam is received. The technique has been applied to the measurements of target velocity and acceleration (Stanbridge and Ewins 1996) (Hollaway and Cadei 2002) (Levin, Lieven and Skingle 1998), and for detection of delamination in ceramic tiles (De Andrade, et al. 1999) and composite structures (Vanlanduit, Guillaume and Schoukens 2002) (Ghoshal, et al. 2003) (Amraoui and Lieven 2004) (Williemann, et al. 2004). These previous developments generally dealt with all composite/ epoxy specimens. Reported work also includes the use of sound and focused sound to excite frescos on masonry together with the use of scanning laser for measurements (Castellini, et al. 1998). In these tests, the excitation source was in contact or in close range with the sample either at the top or side edge, and the method relied on the propagation of sound waves through the material to the damaged area. Furthermore, this development was not particularly developed for application to the NDT of FRP-steel systems.

1.5 Objective and Approach

The objective of this research is the use of acoustic LDV to locate and geometrically size defects on the composite-steel interface. The research approach involved a review of current NDT methods, the use of both theoretical and numerical analyses, as well as laboratory experiments as a basis for validation of the research objective. The review of current NDT methods revealed a clear capability gap with respect to robust standoff methods. Experimental measurements of a debonding defect on the FRP-steel interface were conducted using acoustic LDV. A parametric study of the system was performed and defect mappings were created. This was then compared with the results from theoretical and numerical (finite element) methods in order to validate the methods.

2 The Acoustic Laser Method

Acoustic LDV is a relatively new method of NDT that shows a lot of promise in use on civil and naval structures. In this approach, an airborne acoustic wave is used to excite the direct location of the damage underneath the FRP sheets/plates and in the substrate using a focused

sound beam, and measure the target vibration using laser Doppler vibrometry. The sound needs to cover a large bandwidth to ensure that all frequencies of interest are included. Defects or heterogeneities within the structure will cause a locally increased response. From the increased response the size and nature of the defect can be estimated. This method of NDT is especially useful where two materials are joined together and hence has great potential for the use on composites bonded to steel. This potentially revolutionary method is robust yet simple and can produce high resolution results. The acoustic laser method depends on two theoretical bases: the coupling of the acoustic airborne sound to the structure and the theory describing the vibration of the defective part of the plate.

2.1 Sound Coupling to Structure

It is observed that airborne acoustic waves may couple to structures and generate a vibration field over the surface of the structure. Local heterogeneities in the structure can cause local vibration anomalies that are a function of the heterogeneity dimensions and mechanical properties. These vibration anomalies can be measured at the target surface using a laser vibrometer, and thus, the target's heterogeneities can be remotely detected, mapped, and quantified. When acoustic waves come into contact with solids, most of the energy reflects back into the air. A small percentage of these waves, however, couples to the solid, causing motion that transmits a series of waves as shown in Figure 9. These waves consist of a surface wave (the Rayleigh wave) that travels at the air/solid interface, and body waves that travel into the solid (shear and compressional waves). The Rayleigh wave travels along the boundary of the FRP and air. At a specific frequency, the Rayleigh wave will produce a resonant response in the FRP that is a function of the void or crack dimension. The Rayleigh wave over a finite length void can be described as a standing wave in terms of two harmonic waves traveling in opposite directions:

$$y(x,t) = Ae^{j(\omega t - kx)} + Be^{j(\omega t + kx)} \tag{1}$$

where y is the vibration amplitude as a function of distance along the void, x, and time, t, A and B are complex amplitudes that are determined by the boundary conditions, k is the wave number, and ω is the angular frequency. A standing wave may form along the length of the void, L, where its wavelength, λ, forms nodes and antinodes at half wavelengths and forms resonances at n frequency harmonics:

$$f_{rn} = \frac{2n-1}{4}\frac{c}{L} \tag{2}$$

where f_{rn} is the cyclic frequency, c is the acoustic waves speed, and L is the length of the void or extent of the delamination.
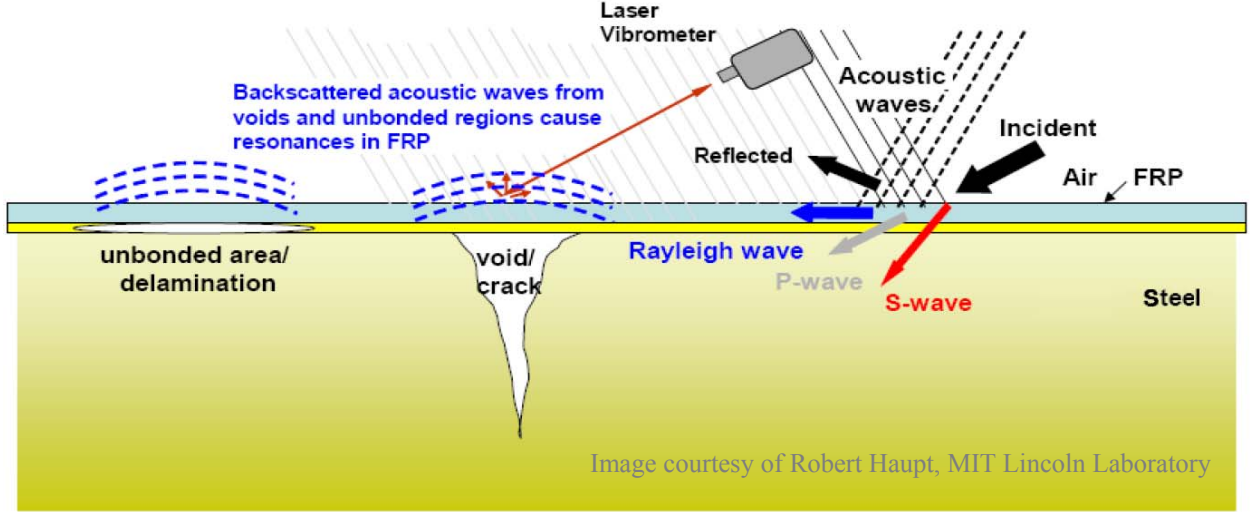
Figure 9: Acoustic coupling to FRP structures adapted from Buyukozturk et al (2011)

2.2 Simplified Beam and Plate Vibration Models

Unnoticed cracks and voids can occur in the FRP-metal joint during the manufacturing or repair process. These existing and/or new cracks may further develop, due to excessive loading conditions, while in service and lead to delamination or debonding between the FRP and the substrate material. Simplified models are established and illustrated in Figure 10 to characterize the difference between intact and damaged regions in the vicinity of the FRP-metal material interface.
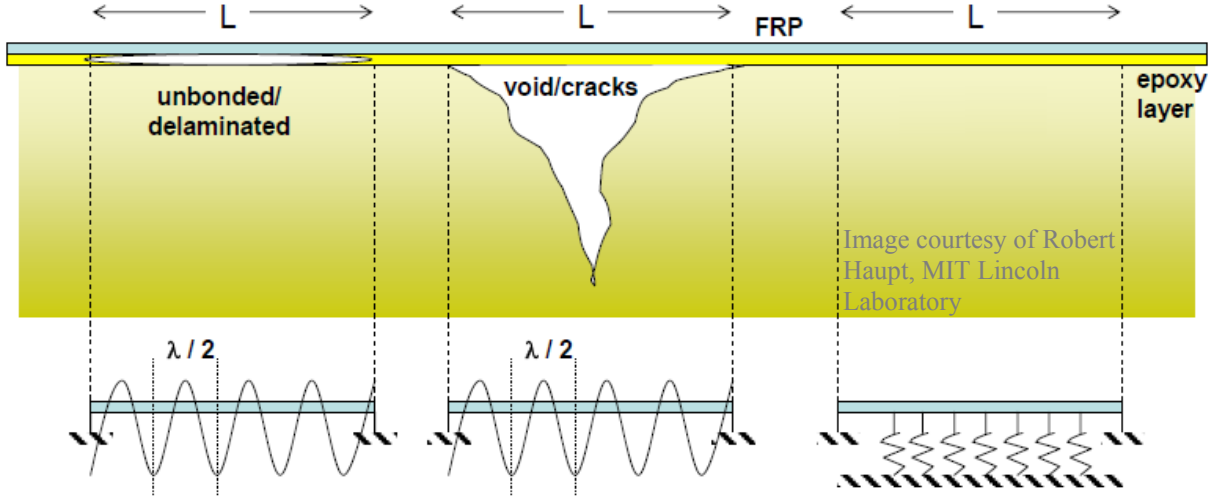
Figure 10: Simplified model of damage in FRP-metal structures adapted from Buyukozturk et al (2011)

To describe the vibration of the damaged and intact regions of the structure first a simple two dimensional case was considered. Here the FRP layer above the delamination or other defect is modeled as a beam with fixed boundary conditions which has the governing equation of motion in free vibration of:

$$EI\frac{\partial^4 y}{\partial x^4} + \rho A\frac{\partial^2 y}{dt^2} = 0 \tag{3}$$

where E = Young's modulus, I = moment of the inertia, ρ = density of the material, A = cross sectional area, $y = y(x,t)$ = transverse displacement of the beam at position x and time t. The natural frequency of the *i-th* mode for the damaged structure $(\omega_{void})_i$ is found by solving Equation 3 using the method of generalized coordinates:

$$y(x,t) = \sum_{i=1}^{\infty} \varphi_i(x)q_i(t) \tag{4}$$

$$(\omega_{void})_i = \sqrt{\frac{K_i}{M_i}} = \sqrt{\frac{EI \int_0^L \left[\frac{d^2 \varphi_i(x)}{dx^2}\right]^2 dx}{\rho A \int_0^L \left[\frac{d\varphi_i(x)}{dx}\right]^2 dx}} \tag{5}$$

where K_i = the generalized stiffness of the *i-th* mode, M_i = the generalized mass of the *i-th* mode, $\varphi_i(x)$ = shape function, and $q_i(t)$ = generalized coordinate. Similarly, the governing equation of motion of the intact structure is:

$$EI \frac{\partial^4 y}{\partial x^4} + \rho A \frac{\partial^2 y}{\partial t^2} + ky = 0 \tag{6}$$

where k = distributed stiffness coefficient characterizing the connection between the FRP and the metal. The natural frequency of $i\text{-}th$ mode for the intact structure ω_i is found by:

$$\omega_i = \sqrt{\frac{K_i}{M_i}} = \sqrt{\frac{EI \int_0^L \left[\frac{d^2\varphi_i(x)}{dx^2}\right]^2 dx + \int_0^L k[\varphi_i(x)]^2 dx}{\rho A \int_0^L \left[\frac{d\varphi_i(x)}{dx}\right]^2 dx}} \tag{7}$$

The absence of connection between the FRP and the metal which is characterized by the $\int_0^L k[\varphi_i(x)]^2 \, dx$ term, will decrease the natural frequency of the system.

While this simplified model using beam theory is acceptable for an initial discussion of the vibration of the defective and intact regions of the structure, a deeper investigation through plate and shell theory is required. Making much the same argument as was made for beam theory model; the defect is modeled as a plate with some boundary condition (fixed or simply supported) around the edge of the plate covering the defect as shown in Figure 11.
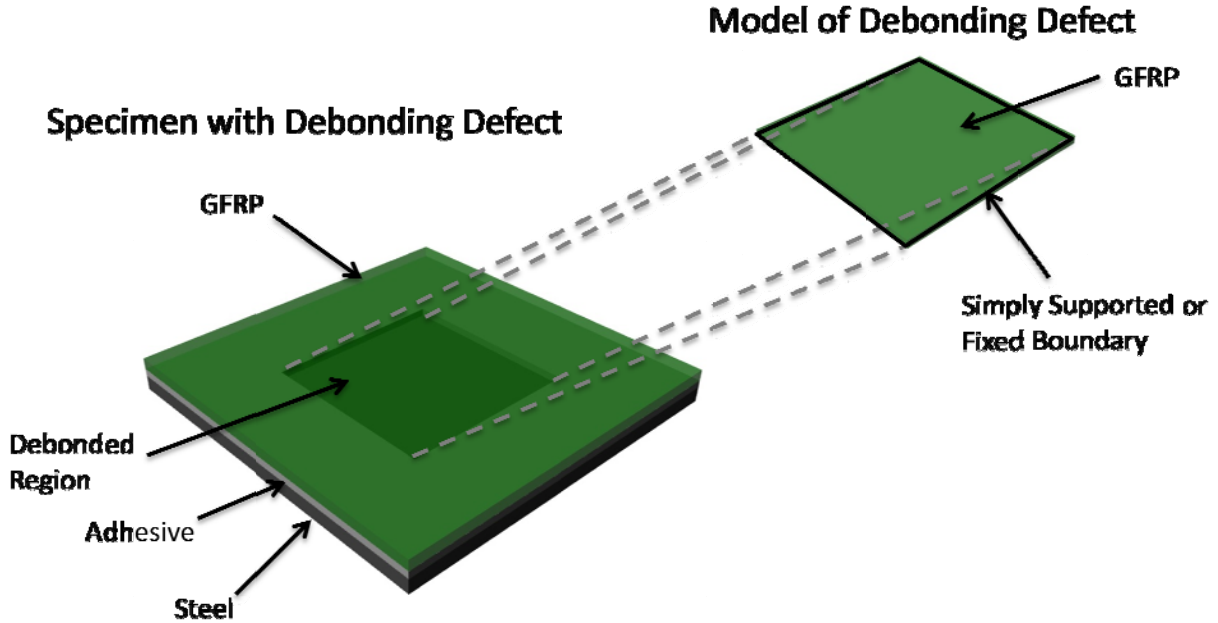
Figure 11: Sketch of model of debonding defect showing area above defect that is modeled. A square defect is shown here but the same model can apply to any shape of defect.

Much of the following is general vibration mechanics knowledge but this solution method is from *Vibration of Plates* (Leissa 1969). The governing equation for the free vibration of the plate is given by:

$$D\nabla^4 w + \rho h \frac{\partial^2 w}{\partial t^2} = 0 \qquad (8)$$

where D= flexural rigidity given by:

$$D = \frac{Eh^3}{12(1 - v^2)} \qquad (9)$$

E = Young's modulus, h = plate thickness, v = Poisson's ratio, $w = w(x,y,t)$ = transverse displacement, ρ = density of the material, t = time, and $\nabla^4 = \nabla^2\nabla^2$ where ∇^2 is the Laplacian operator. Similarly the governing differential equation for the intact structure is defined by:

$$D\nabla^4 w + Kw + \rho h \frac{\partial^2 w}{\partial t^2} = 0 \qquad (10)$$

where K is the stiffness of the intact supporting structure beneath the FRP characterizing the connection between the FRP and metal with some form of epoxy. Regardless of whether the plate is part of a defect or intact structure, the solution takes the same form. The motion of the plate will take the form:

$$w = W\cos(\omega t) \qquad (11)$$

where ω is the circular frequency (in radians/unit time) and W is a non-temporal displacement function of the position under consideration. Using the definition that k depends on whether the plate has a foundation giving it stiffness:

for the unsupported (defect) case: $k = \frac{\rho h \omega^2}{D}$

for the supported (intact) case: $k = \frac{\rho h \omega^2 - K}{D}$

In either case when substituting into the original differential equation for the free vibration of a plate gives:

$$(\nabla^4 - k^4)W = 0 \qquad (12)$$

And Equation 12 can be factored to give:

$$(\nabla^2 + k^2)(\nabla^2 - k^2)W = 0 \qquad (13)$$

By the theory of linear differential equations the solution to Equation 13 can be found by superimposing the solutions to the equations:

$$\nabla^2 W_1 + k^2 W_1 = 0 \tag{14}$$

$$\nabla^2 W_2 - k^2 W_2 = 0 \tag{15}$$

Defining the solution of the eigenvalues and natural frequencies of plates is based on the shape and boundary conditions of the plate so it is difficult to give a general solution that works for all plates in any coordinate system. This discussion will focus on elliptical plates as that is the shape of the defect specimen that was created, but it will also consider rectangular plates as they were used to determine what size of defect specimen to create.

Of particular interest in this study is the vibration of elliptical plates since that is the shape of the defect specimen studied. The classical solution to an elliptical plate requires first defining elliptical coordinates ξ and η which are related to rectangular coordinates x and y by the equation:

$$x + iy = c \cosh(\xi + i\eta) \tag{16}$$

The complete solution of the motion of the plate is given by:

$$W = W_1 + W_2 \tag{17}$$

which after a significant amount of work and calculation gives:

$$W = \sum_{m=0}^{\infty} [C_m Ce_m(\xi, q) ce_m(\eta, q) + C_m^* Ce_m(\xi, q) ce_m(\eta, -q)]$$

$$+ \sum_{m=1}^{\infty} [S_m Se_m(\xi, q) se_m(\eta, q) + S_m^* Se_m(\xi, -q) se_m(\eta, -q)] \tag{18}$$

where Ce_m, ce_m, Se_m, and se_m are ordinary Mathieu functions of order m; C_m, C_m^*, S_m, and S_m^* are constants of integration; and

$$q = k^2 = \omega \sqrt{\frac{\rho h}{D}} \tag{19}$$

Worth noting is the way in which an elliptical plate will vibrate and the mode shapes it will assume. There are four groups of vibrations that can occur: symmetric about both axes; antisymmetric about both axes; symmetric about the major axis and antisymmetric about the minor axis; antisymmetric about the major axis and symmetric about the minor axis. Depending

on whether the mode shapes of the elliptical plate are symmetric with respect to both axes (m even) or with respect to the minor axis (m odd), the solution reduces to:

$$W = \sum_{m=0}^{\infty} [C_m Ce_m(\xi, q)ce_m(\eta, q) + C_m^* Ce_m(\xi, q)ce_m(\eta, -q)] \tag{20}$$

However, if the mode shapes are antisymmetric about both axes (m even) or with respect to the major axis (m odd), the solution reduces to:

$$W = \sum_{m=1}^{\infty} [S_m Se_m(\xi, q)se_m(\eta, q) + S_m^* Se_m(\xi, -q)se_m(\eta, -q)] \tag{21}$$

When the roots of Equations 20 and 21 are taken, the following relation for the modal frequencies is shown to be:

$$\omega = \frac{\alpha}{ab}\sqrt{\frac{D}{\rho h}} \tag{22}$$

where a = radius along major axis, b = radius along minor axis, and α is a constant determined by the mode of vibration (square root of the eigenvalue) by solving for the roots of the determinant of the motion equation. In different sources, α can be found to be called λ^2 or Ω but throughout this research α will be used for consistency as this is the notation Timoshenko originally used (Timoshenko, Young and Weaver Jr. 1974). Through various methods including Rayleigh quotient (Shibaoka 1956), Galerkin (McNitt 1962), and Ritz, the values for α have been tabulated by both Leissa and Rajalingham. Rather than reiterate the calculations they have done as it is outside the scope of this research, the values for α they determined will be considered the accepted theoretical values.

Values for α are tabulated for a variety of boundary conditions and plate shapes. Here the values considered account for a major to minor axis ratio (a/b) of 1.2 as this is very close to the values actually seen in the specimen that was constructed. The values for α used were developed by Rajalingham (1991) and are shown in Table 1.

Table 1: Values of constant α for first five modes of vibration of an elliptic plate with different boundary conditions (Rajalingham, Bhat and Xistris 1995) (Rajalingham and Bhat 1991)

Mode	α (Simply Supported)	α (Fixed)
1	5.055	10.461
2	14.030	19.735
3	15.568	23.615
4	23.847	32.625
5	26.015	35.516

Based on these values of α, the frequency of each mode of vibration can be calculated based on Equation 22 and are listed in Table 2. Although the boundary at the edge of the plate covering the defect is assumed to be fixed, simply supported boundary conditions were also calculated to ensure that the actual measured frequency values fit within the range of possibilities between simply supported and fixed. It should not be possible for the actual measured results to be less stiff than simply supported or stiffer than fixed boundary conditions.

Table 2: Frequency of first five modes of vibration of an elliptic plate

Mode	Frequency [Hz]	
	Simply Supported	**Fixed**
1	1351	2795
2	3748	5272
3	4159	6309
4	6371	8716
5	6950	9488

The majority of the values of α tabulated by Leissa (1969) were in reference to circular and rectangular vibrating plates. While the actual specimen that was created ended up being elliptical, rectangular values were used to determine the size of defect to construct. For the determination of defect size, square defects (and therefore plates) with side lengths of 7.62 cm (3 in), 15.24 cm (6 in), and 22.86 cm (9 in) were considered. The generalized solution to the vibrating square plate takes much the same form as the elliptical plate. The major differences are in the use of Cartesian coordinates and the treatment of different boundary conditions. However, the same format of result is developed where for a square plate:

29

$$\omega = \frac{\alpha}{a^2} \sqrt{\frac{D}{\rho h}} \qquad (23)$$

which is essentially the same equation as seen for the elliptical plate (Equation 22) except instead of having the characteristic dimensions being the major and minor axis radii; here the characteristic dimension is the side length of the square plate, a. The values for α for the first mode of vibration for square plates are $\alpha = 35.999$ for a plate with fixed boundary conditions on all sides and $\alpha = 19.87$ for a plate with simply supported boundary conditions on all sides. These values were used to confirm some of the finite element results that were used to determine what size of defect specimen to create.

Additionally, the equations solving for the fundamental frequency can be used to solve for the size of the defect given the frequency calculated. A spreadsheet was created using the various α values for elliptical, square, and circular defects into which the first modal frequency can be entered and the output will be the approximate size of the defect depending on boundary condition and shape. A tool of this type would prove very valuable for the development and employment of the acoustic laser method in on-site NDT scenarios.

3 Numerical Analysis

For numerical analysis, the finite element method was utilized (ADINA R & D, Inc. 2011). Initially, finite element analysis was used to help determine the size of defect that would give the best results with the laser vibrometry measurement equipment. Next it was used to compare with theoretical and measured results to ensure an appropriate correlation was seen. Within the finite element analysis, comparisons of solid elements to shell elements were made as well as what type of boundary conditions to set. The boundary conditions were assumed to be fixed in most cases but in reality the boundary condition on the edge of the defect region is actually something between simply supported and fixed as was shown through this analysis. The defect was modeled the same as the theoretical analysis as the plate covering the debonding with some boundary condition around the edge as shown in the sketch in Figure 11.

3.1 Delamination Defect Size Determination

The first finite element analysis that was done was to determine the size of the defect to be used for experimental measurements. The best way to analyze various size defects was to use

three dimensional (3D) solid elements so that the size of the defect did not impact how well the elements performed. This could have been an issue had shell elements been used since for small defects the FRP plate above it is not a thin shell at all but responds more like a three dimensional solid material. The 3D elements used had 27 nodes. The 27 node elements allow for best capturing how curved edges will react. While the initial defect decision was done with only square defects, the 27 node element was chosen for consistency with other circular or elliptical defects that were evaluated.

Before a model could be created of just the plate above the defect, a model had to be made to determine if there was any interaction between the FRP plate and the steel plate. This was done by creating the two plates in the finite element program. The largest size of defect that was deemed worth creating from the 0.3048 m (12 in) square plates was 0.2286 m (9 in) square. This was chosen so that the defect could be analyzed without any effect from the edge of the plates. The largest defect will have the greatest deflection of the FRP for the same load and therefore the greatest chance of it contacting the steel in the absence of the epoxy bonding the two materials together. For the finite element model, only the material above and below the defect was modeled. The model consisted of a 0.2286 m (9 in) square plate of 5 mm (0.2 in) thick FRP with a 0.1 mm (~4 mil) air gap between it and a 0.2286 m (9 in) square plate of 9.5 mm (0.375 in) thick stainless steel. The edges of both plates were given fixed boundary conditions. This assumption was made since the defect (delaminated) portion of the plate is unsupported and therefore resembles a fixed boundary where the plates are joined by epoxy.

The maximum displacement of the FRP material, when a very high sound pressure level of 150 dB (~600 Pa) was applied, was found to be 25 μm as shown in Figure 12 which is significantly less than the distance between the two materials of 100 μm (~4 mil). The normal sound pressure level used during experimental measurements is around 80 dB (0.2 Pa). This means that for any size defect (delamination) considered, the FRP will not contact the steel. Therefore, a model of only the FRP material will capture the response of the structure due to the delamination defect. This significantly reduces the amount of computational time required for the finite element analysis portion of this research. All future models discussed will be of only the FRP plate unless otherwise specified.
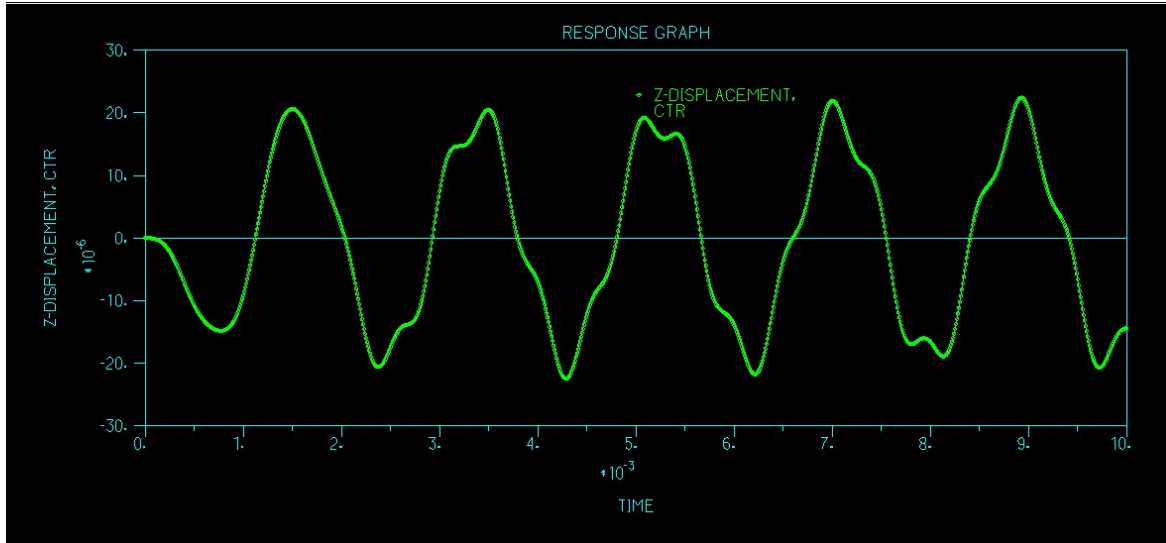
Figure 12: Displacement time series at center of square defect with a sound pressure level of 150 dB applied as a frequency sweep

The responses of three different sizes of defect were compared to determine which had the best response with potential for measurement with the acoustic laser Doppler vibrometry equipment. Delamination defect sizes considered were square with edge lengths of 7.62 cm (3 in), 15.24 cm (6 in), and 22.86 cm (9 in). The defects were analyzed with just the FRP plate due to no contact effects as discussed above. For this analysis, 3D solid elements were used with fixed boundary conditions. The first mode of vibration was compared in all cases to gauge how well the defect size would work for the experimental measurements using the acoustic LDV system. The first mode was also calculated using theoretical tabulations from Leissa (1969). The first mode gave a good indication of how "measureable" the specimen would be when actually built; the issue being the limit of what the acoustic LDV system can measure. A cutoff of about 300 Hz was used when doing measurements so that low frequency noise (e.g. 60 Hz electrical and harmonics) would not be measured, so too low of a frequency of vibration for the first mode could be an issue. Also too high of a first modal frequency would not allow for enough higher modes below the 20,000 Hz acoustic laser system cutoff to best describe the defect. Table 3 shows the first modal frequencies from both theoretical calculations and finite element analysis. The 15.24 cm defect was chosen since it gave the lowest frequency of the first mode that was still well above the 300 Hz low frequency cutoff. It is important that the frequency be well above this cutoff because there was some uncertainty in the accuracy of these

32

estimates prior to making any physical measurements and there could be inaccuracies in constructing the specimen that could lead to a different frequency than was intended.

Table 3: Frequency of first mode of vibration for three different square defect sizes

	Frequency of 1st Mode (Hz)		
Side Length	Theoretical	Finite Element	% Difference
7.62 cm	4207	4678	10.60%
15.24 cm	1052	1211	14.05%
22.86 cm	467	543	15.05%

3.2 Finite Element Type Comparison

The element used to determine defect size was a three dimensional solid element due to uncertainty in the thickness of the plate when compared to its other dimensions. In order to use a shell or plate element, the structure must be thin in one dimension and it is assumed that the through thickness stress of the plate/shell is zero and that material particles originally on a straight line perpendicular to the midsurface remain on a straight line during deformations (Bathe 2006). Since the analysis using sound pressure waves keeps the structure well within the elastic range and the pressure is evenly applied to the entire surface of the defect, through thickness stresses can reasonably be assumed to be zero.

For the elliptical defect that was actually created, finite element models were compared using 3D solid elements and shell elements. The shell element should respond reasonably well as the thickness of the FRP plate is only 5 mm (0.2 in) and the diameter of the ellipse along the major axis is 11.4 cm (4.5 in) and along the minor axis is 8.9 cm (3.5 in). This reasonably passes the definition of the structure being "thin" in one dimension when compared to the other two. Figure 13 and Figure 14 display the 3D element representation and the shell element representation, respectively. It can be seen that using shell elements can allow for a much finer mesh for the same amount of computational power as the solid elements. This is due to the much simpler material matrix considered with the shell element since through thickness effects are ignored. Table 4 shows the comparison of vibration modes using fixed boundary conditions on the edges of the solid and shell elements. The first five modes of vibration are essentially the same for both the solid and shell element models. Beyond the first five modes was not

considered due to difficulty in finding the higher level modes with the laser vibrometry equipment. The similarities in the results from both the solid and shell element models means the shell model can be used going forward. This significantly reduces computation time and gives higher fidelity results by being able to use a finer mesh of elements.
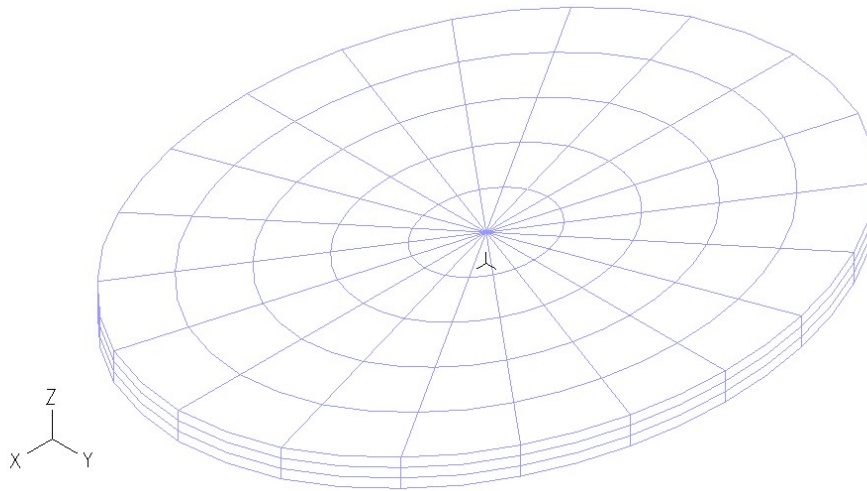

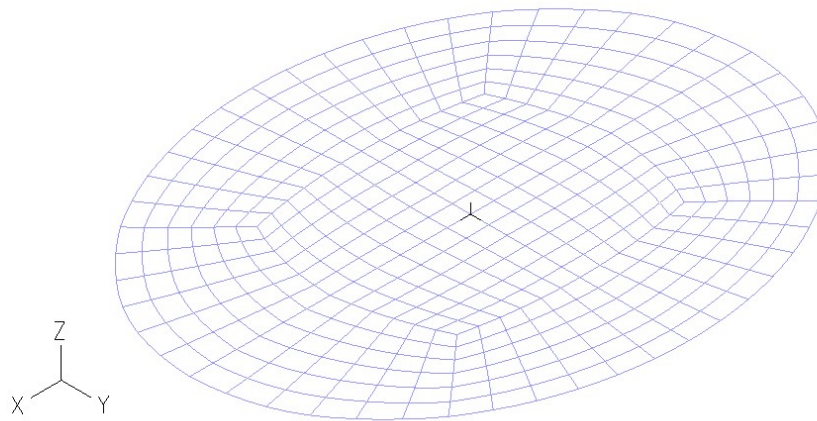**Figure 13: Elliptic defect model showing the use of 27-node 3D solid elements**

Figure 14: Elliptic defect model showing use of 9-node shell elements

Table 4: Comparison of vibration modes of elliptic defect using 3D solid elements and shell elements

Mode	Frequency [Hz] (3D solid)	Frequency [Hz] (shell)	% Difference
1	3044	3036	0.27%
2	5461	5431	0.56%
3	6878	6855	0.33%
4	8773	8686	1.00%
5	9891	9840	0.51%

3.3 Analysis of Crack Defect

The defects analyzed with theoretical and finite element methods to this point have all been delamination defects on the steel-epoxy-FRP interface. Additional effort was made to detect a cracked defect. First a 0.5 m (1.64 ft) square plate of 5 mm (0.197 in) thickness was created with a 0.25 m (9.84 in) by 0.002 m (0.079 in) crack in the center of the plate. The crack extended through the entire thickness of the plate. The plate was modeled using 9-node shell elements since based on the above analysis they give excellent results with minimal computation time. A depiction of the plate with the crack is shown in Figure 15. The modal results from this finite element analysis show that the defect should be noticeable with the laser acoustic method as compared with a solid plate. Table 5 shows the comparison of the cracked and uncracked GFRP plates' modes of vibration. The larger percent errors occur at different modes due to the impact the crack has on the particular mode shape.

Extent of Crack Defect
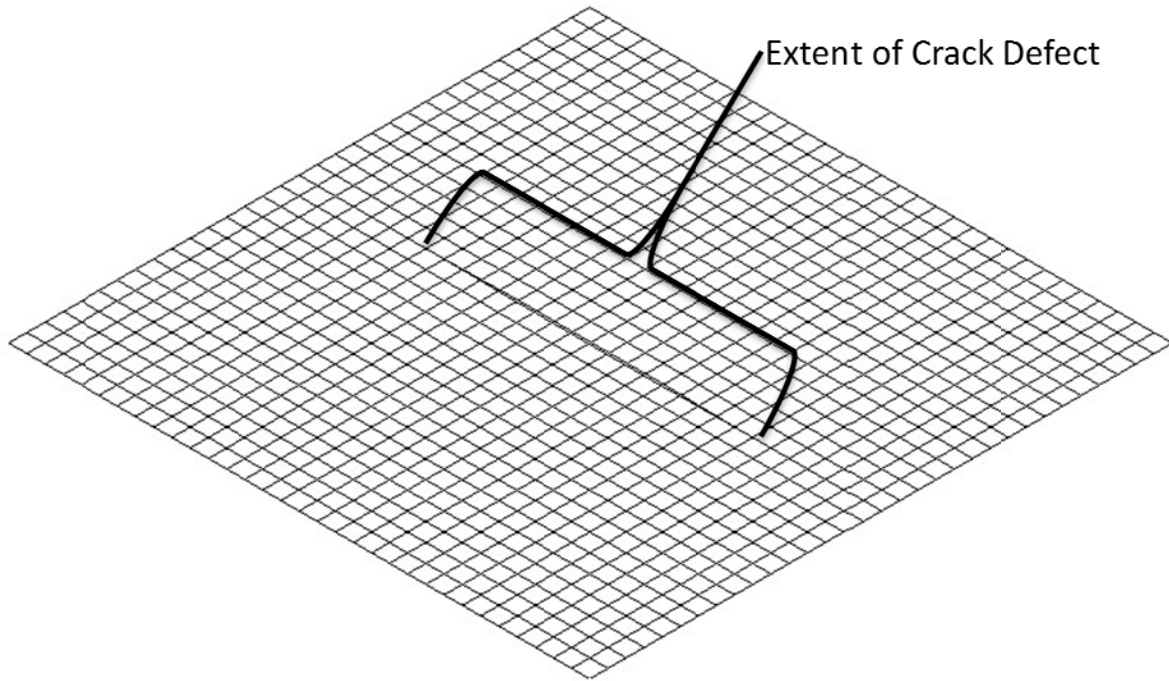
Figure 15: Finite element mesh depicting crack defect in center of GFRP plate

Table 5: Comparison of frequencies of modes of vibration for uncracked and cracked (through full thickness) square GFRP plate

	Frequency [Hz]		
Mode	**Intact**	**Cracked**	**% Error**
1	106.10	97.61	8.00%
2	216.24	173.58	19.73%
3	216.24	213.76	1.15%
4	318.61	308.26	3.25%
5	387.28	328.44	15.19%
6	389.14	353.76	9.09%
7	485.33	386.91	20.28%
8	485.33	463.75	4.45%

A similar analysis was done for steel plates and gave similar results for each mode only having different frequency values. Next a plate was simulated with a crack that only extended to half the thickness of the plate. In this case the same material properties and dimensions of the

36

plate were used (with the exception of the thickness being 6.35 mm (0.25 in)); however, the crack in this case was not noticeable based on a modal analysis comparison to an intact plate as shown in Table 6. The crack through half the thickness allows for the bending stresses due to acoustic excitation to be transferred through the uncracked portion. Since the acoustic excitation remains well within the elastic range of the material, there is no measureable indication that the crack exists when compared to an uncracked specimen of the same size. This was determined by a less than 1% difference between the frequency of a cracked plate and an intact plate.

Table 6: Comparison of frequencies of modes of vibration for uncracked and cracked (through half thickness) square GFRP plate

	Frequency [Hz]		
Mode	Intact	Cracked	% Error
1	138.83	138.62	0.15%
2	290.83	290.72	0.04%
3	290.83	290.78	0.02%
4	429.09	428.98	0.03%
5	546.77	545.26	0.28%
6	548.84	548.01	0.15%
7	674.64	673.34	0.19%
8	674.64	674.48	0.02%

Analysis was also conducted for a steel plate bonded to a FRP plate with a crack through the full thickness in one of the plates. This gives a similar result to what was seen with a plate cracked only halfway through. Again in this case the intact portion is able to transfer the elastic stresses and therefore there is no noticeable difference in the intact and cracked frequencies. While it is unfortunate that it does not appear that small cracks will be detectable with this method due to the large amount of intact structure, at least when cracks extend through the entire thickness of the structure they should be noticeable with the acoustic laser method.

4 Experimentation

4.1 Specimen Preparation

To evaluate the acoustic laser vibrometry NDT method specimens of stainless steel (AL6XN alloy) plate and glass fiber reinforced polymer (E-glass/vinyl ester) were constructed. The stainless steel and GFRP plates were adhesively joined together by epoxy with some form of defect in the bonding. The epoxy used was Loctite Adhesives Hysol E20-HP and was chosen due to its good bonding characteristics with both steel and fiberglass and its viscosity. The viscosity of the epoxy prevented it from self leveling and significantly decreasing the bond line thickness. The specimens were 0.3048 m (1 ft) square with a steel plate thickness of 9.525 mm (3/8 in), GFRP thickness of 4.7625mm (3/16 in), and bond line thickness of roughly 100 μm (~4 mils = 0.004 in).

To prepare the bond surface the stainless steel plate was abraded with varying roughness sandpaper (100 - 220 grit) until the surface appeared to be smooth and uniform. Then the surface of both plates was wiped clean using acetone. With both surfaces clean the epoxy was applied using a mixing tip on a discharge gun which made for easy application. The epoxy beads were smoothed with a plastic putty knife to achieve as uniform a layer as possible. It is important to note that when applying the epoxy, special care was taken to ensure a portion of both plates had no epoxy which created the defect in the bond. For the initial specimen a 0.1524 m (6 in) square area was left free of epoxy in the center of both the stainless steel and GFRP plates. Once the areas on both surfaces to be bonded were fully wetted the GFRP plate was placed on top of the steel one. Then the two pieces were clamped together to ensure a full bonding all around the defect as shown in Figure 16.
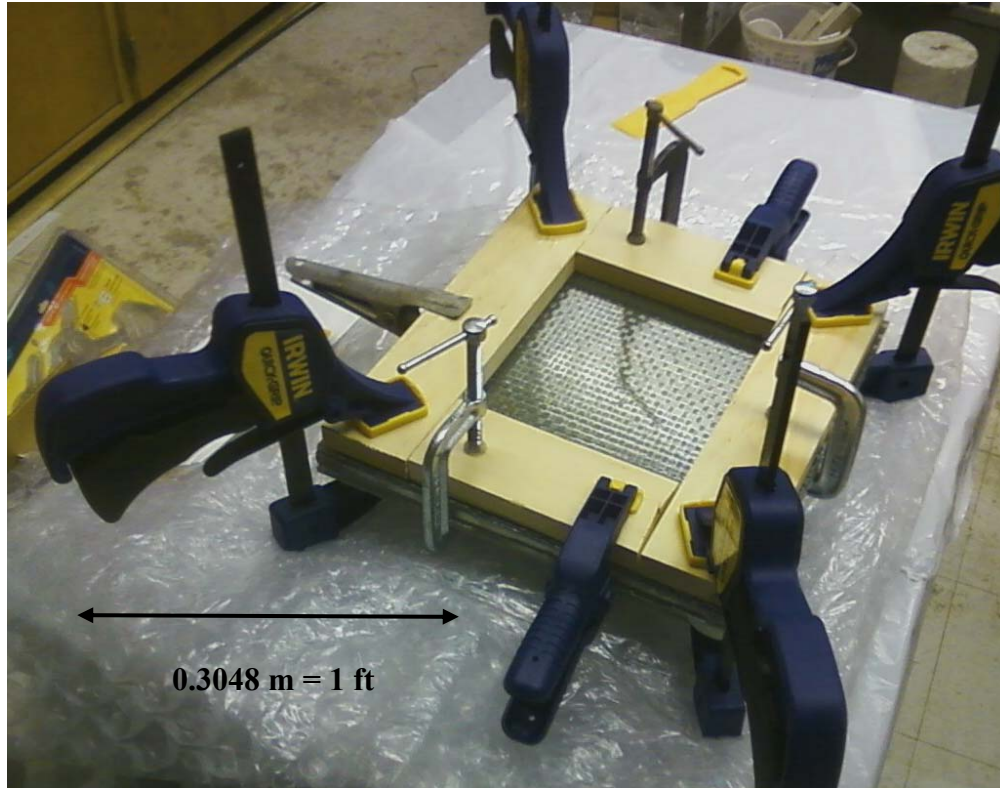
Figure 16: Specimen construction showing clamping of edges to ensure only a central defect

After the epoxy cured for 24 hours the defect visibly appeared to be an ellipse shape with an approximate size of 11.43 cm (4.5 in) on the major axis and 8.89 cm (3.5 in) on the minor axis. This was determined visibly by noticing the color difference in the GFRP between the bonded and debonded regions. This proved to be an unplanned advantage of using GFRP by allowing the defect to be visually seen which would not have been possible had a different composite material (e.g. carbon fiber) been used. Also the intended shape of the defect was to be a square shape but due the pressure applied by the clamps the epoxy seeped in toward the center of the specimen more than was expected creating the ellipse. However, there is a good theoretical basis for the vibration of elliptical plates so it was acceptable for use in this research.

4.2 Experimental Procedure

The specimen with defect was tested nondestructively using the acoustic laser Doppler vibrometry equipment available at MIT Lincoln Laboratory. The equipment setup utilized a Polytec laser vibrometer, speaker (subwoofer), laptop computer, Wavebook waveform acquisition, and microphone as shown in Figure 17. Prior to measurement, pieces of retro-reflective tape were attached to the GFRP surface in order to get a better return from the laser

above the noise floor and also to discretize the defect into a set of points from which measurements can be taken and tracked. This is not realistic to a real world measurement scenario, but a better laser as would be used for real world measurements would have better resolution and not require the tape applied prior to measurement. The panel was leaned against a wall on its edge with the GFRP side facing out. The plane of the panel was perpendicular to the laser and speaker so as to have the best response and to remove the impact of the incident angle of either the sound or the laser. The laser was approximately 2 m (6.56 ft) away from the panel while the speaker was approximately 1.5 m (4.92 ft) away from the panel. The speaker and laser were located on different tables so that the vibrations from the speaker would not cause the laser base to vibrate. This was very important in order to keep the measurement noise floor as low as possible.
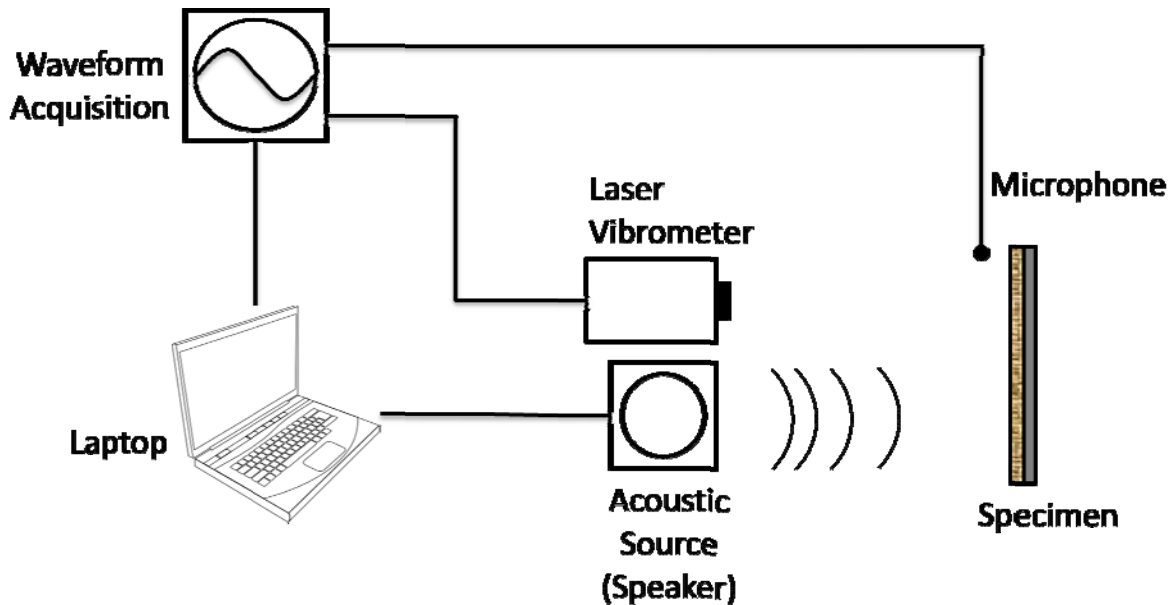

Figure 17: Line diagram of experimental measurement setup

A number of different measurements were made in order to show the differences in the response of the panel. First to simply realize a response a series of points starting at the center of the defect and radiating outward along the major and minor axes of the elliptic defect were measured using a 10 s acoustic frequency sweep from 0-20 kHz. At each point a background (no sound) and at least one frequency sweep were measured.

Next a set of measurements were completed to compare the response of the defective part of the panel to the sound pressure level. To be more exact with these measurements, the first

mode of vibration was found based on previous data and then instead of using a sweep, a 10 s tone of just the frequency that excites the first mode was played.

Another set of measurement comparisons were the length of time it took to sweep from 0-20 kHz. Sweeps of 60, 10, 1, and 0.1 seconds were completed for comparison. The sweep of 0.1 s was constantly repeated to make the timing of taking the measurement easier. A 60 second white noise signal was played to compare the response of white noise to that of a frequency sweep.

Additional parameters such as the incident angle of the system to the specimen were checked. Another parameter measured used a set of neutral density (ND) filters to reduce the amount of laser light passing to make a comparison with the laser's operable range. Since ND filters reduce the intensity of light across all wavelengths (380-740 nm) and the Polytec laser's wavelength (633 nm) is in the visual range this is a valid measurement. Also a grid was set up on the surface of the specimen with retro-reflective tape and then measurements were taken to create a mapping of multiple modes of vibration.

5   Results/Discussion

5.1 Data Analysis

The first item to be determined via measurement is that the debonding defect can be visualized with this method as is expected based on theoretical and finite element analyses. To do this a 0-20 kHz frequency sweep was used for acoustic excitation of the specimen. The laser vibrometer was used to measure a spot at the center of the defect and a spot on the intact region off the defect. The sound pressure level was held constant at 78 dB re 20 µPa for both measurements. Figure 18 shows the output response of the measurements on the intact region (a) of the specimen and on the defect region (b). The response on the defect is clearly higher at the various modal frequencies of the defect. The first mode of vibration of the defect region occurs around 2500-2550 Hz. Numerous higher modes of vibration can also be seen on the defect and these will be considered during mapping analysis. There is a response peak lower than this at around 800 Hz, but this is actually the frequency of the entire specimen vibrating with free boundary conditions. Therefore that response can be neglected, as can the straight vertical lines on the plots as those are speckle which results from this laser system.
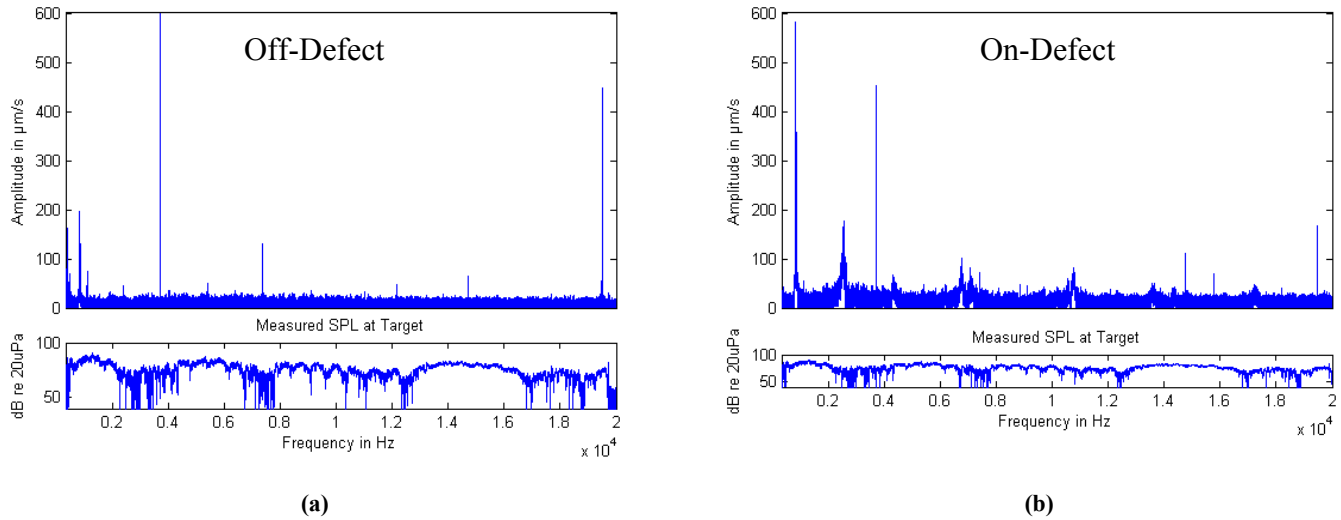
41

Figure 18: Comparison of outputs off debonding defect (a) and on debonding defect (b)

5.1.1 Sound pressure level effect on vibration level

To compare the effect of sound pressure level on the response magnitude, a 10 second tone at 2500 Hz was used. This frequency is approximately that of the first mode of vibration that was discovered from the previous frequency sweeps of 0-20 kHz. The response was measured at the center of the defect to have the highest response at all sound levels. A number of adjustments were made to the volume level of the sound coming from the speaker. A plot of the results is shown in Figure 19. When the sound pressure level is in units of Pa and not dB, a linear relationship is seen between the sound pressure level and the vibration velocity of the defect area. This plot is specific for this defect size and material but other defects will show a similar trend. This is promising for this method of NDT as any size of debonding defect should be detectable with the right amount of sound pressure delivered to the defect area.
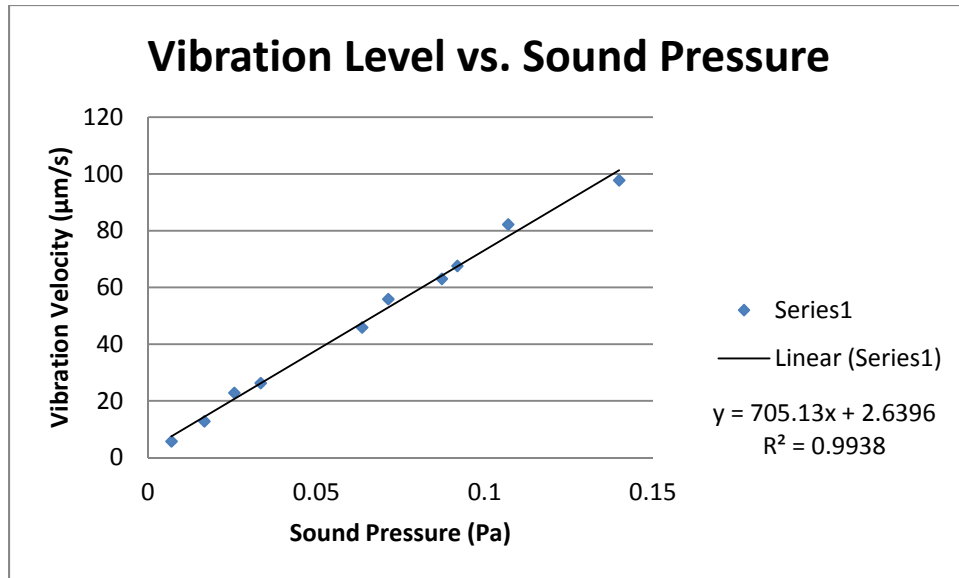
Figure 19: Vibration Amplitude vs. Sound Pressure for elliptic debonding defect

5.1.2   Sweep Duration

As with any NDT method the speed at which an area of a structure can be tested is crucial for productivity. To test this, acoustic LDV was used on the elliptic defect specimen with varying time durations of the frequency sweep from 0-20 kHz. The time of the sweep was varied from 60 seconds to 0.1 seconds. The frequency response was plotted for each and the maximum at the resonant frequency near 2535 Hz was picked. It can be seen from the plots in Appendix A that the vibration velocity amplitude does not change with the changing time of the sweep until the sweep reaches 0.1 seconds. At this rate the sweep is simply too fast to capture the response with the equipment setup currently being used (Figure A4). However, when the 0.1 second sweep is repeated continuously, the response can be seen by only capturing a 0.1 second portion of the response (Figure A5). This is valid because even if the 0.1 seconds selected for analysis does not start and stop at exactly 0 and 20 kHz, respectively, since the sweep is constantly repeating it will cover all the frequencies. A summary plot of vibration amplitude compared to sweep time is shown in Figure 20. It shows the near constant magnitude of the vibration amplitude regardless of the frequency sweep length. This is very promising for the potential productivity of this device in a real world environment. If the linear sweep can be continuously played, then the laser can simply be aimed from spot to spot and take response measurements that do not need to last for more than 0.1 seconds.
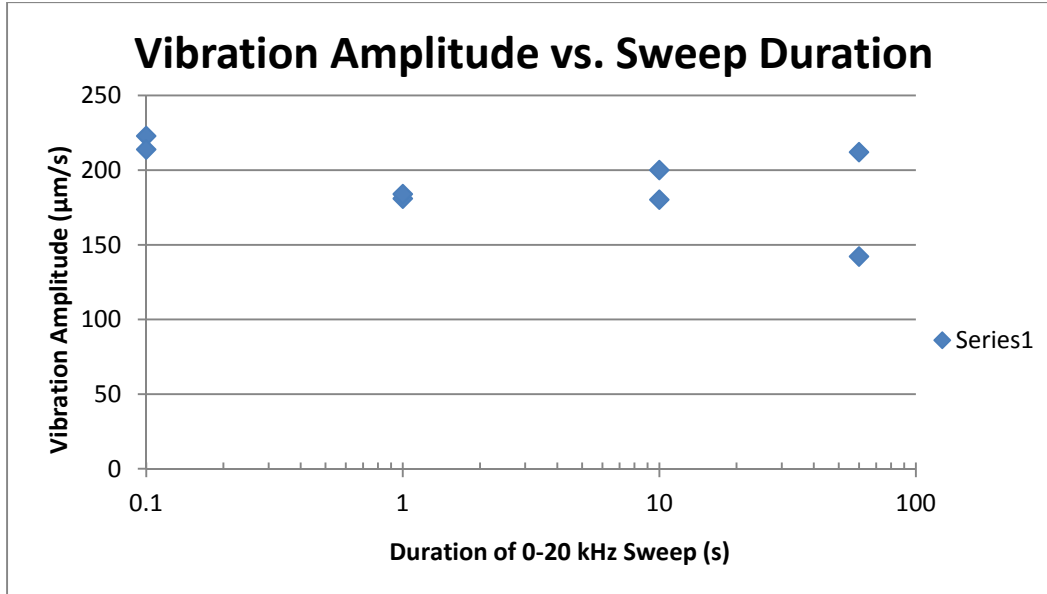
43

Figure 20: Comparison of 0-20 kHz sweep duration to vibration amplitude

5.1.3   White Noise Measurements

Measurements were also taken using white noise to induce vibrations in the specimen defect. White noise induced vibrations do not have as refined a response as the sweep measurements but white noise is beneficial for covering all frequencies at the same time. However, the minimal power that is supplied at each frequency leads to a much lower response magnitude when compared to a sweep. Also the white noise response breaks down as the time duration that is captured decreases. This is due to the time further limiting the amount of power that can be seen at each frequency. An example of the white noise frequency response of the specimen is shown in Figure 21 with a complete set of white noise frequency response plots given in Appendix B. It was determined that going forward white noise measurements would not be of high enough quality to use for defect detection.
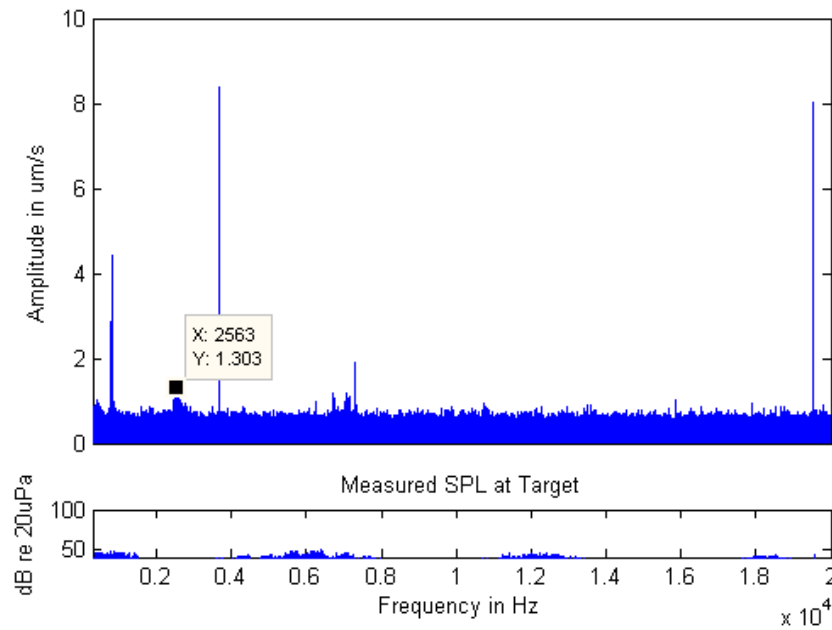
Figure 21: Example of frequency response captured from white noise acoustic excitation (note: much smaller peaks than above with a 0-20 kHz frequency sweep)

5.1.4 LDV System Incident Angles

Experiments were also done to evaluate the effectiveness of the LDV system at various incident angles to the specimen. The goal of this evaluation was to determine the effective angles at which the system can be employed which will show how best to operate the system in a real world situation. This was done using both a 10 second single tone at the resonant frequency as well as a 10 second 0-20 kHz frequency sweep as shown in Figure 22. The results show a relationship between incident angle and vibration amplitude that is a sine squared function and a sine squared curve is shown on the plots for comparison. The sine squared relationship comes from the impact of the angle of the specimen to the incident sound waves and laser beam. The incidence of both leads to the squaring of the sine function. The results closely follow the sine squared relationship between sound pressure level and vibration velocity. The critical angle is reached at a certain point where the return from the specimen can no longer be distinguished above the noise. This angle was different for the resonant frequency tone and the frequency sweep with the sweep being indistinguishable at a greater angle than the tone. For this particular specimen the sweep could no longer be distinguished once the angle decreased below 30 degrees (30 degrees had a high noise floor) while the tone could be distinguished all the way to 15 degrees. This was expected since the tone has all its power focused at one specific frequency

45

while the sweep's power is more spread out. To ensure adequate results it is recommended that the incident angle of the LDV equipment to the structure being analyzed be kept above 30 degrees.
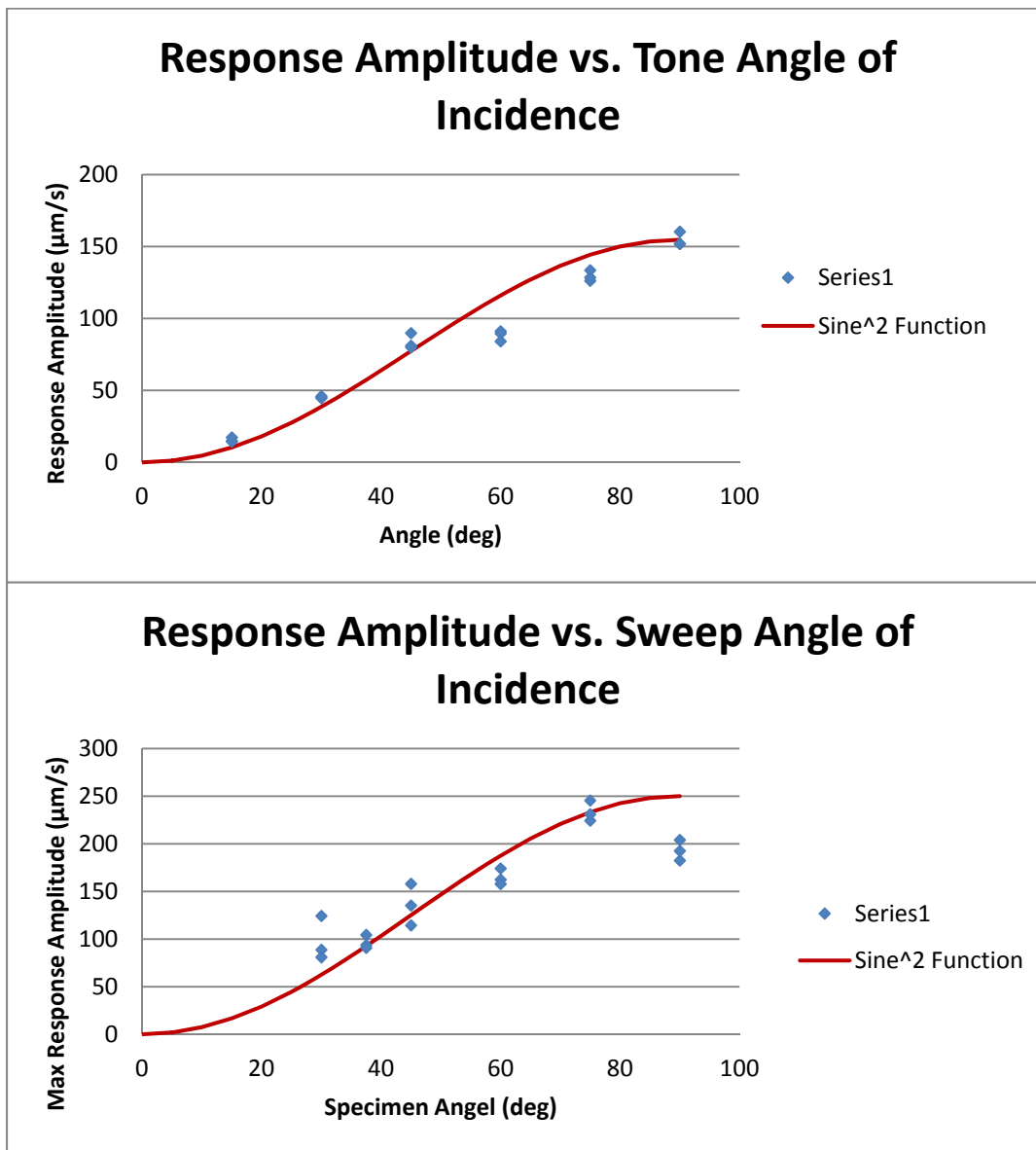

Figure 22: Response Amplitude vs. Acoustic Laser Vibrometer system incident angle to specimen for a 2500 Hz tone (top) and a 0-20 kHz frequency sweep (bottom)

5.1.5   Acoustic LDV System Range

To determine the range of the LDV system, filters were used to change the noise level of the laser return. This replicated changing the distance between the laser and the specimen without physically moving the specimen or LDV equipment. Changing the level of the filter used with the laser changed the amount of light that was able to be transmitted to the specimen

and returned reflecting off the specimen. This shows itself in the measurements as a change in the noise floor of the frequency response. The measurements taken to show this were done using a single tone of 2500 Hz to excite the resonant frequency and therefore have a noticeable response regardless of the noise floor level. The filters showed a log-log relationship between the amount of light able to pass (filter strength) and the noise floor. The equation of the log-log relationship is given by:

$$\log y = -1.431 \log x - 1.979 \tag{24}$$

This equation is illustrated in Figure 23. This is significant to know how much the noise floor changes depending on the amount of attenuation in the laser beam. Depending on the atmospheric conditions where the measurements are taken can determine the maximum effective distance of the laser. A brief analysis was done to determine the laser's attenuation over distance to compare this to the noise floor. It is assumed that once the noise floor is greater than 90 µm/s, it would be very difficult if not impossible to pick out the peak response. A noise floor of 90 µm/s equates to 0.18% of the light that left the laser returning reflected off the specimen. Based on typical attenuation coefficients given by McCartney (1976) for clear air, hazy, and fog conditions, an estimate of where the laser's return would be 0.18% the power of that originally transmitted was determined (Kim, McArthur and Korevaar 2001). For the purposes of this thesis, haze is defined as particle or water droplet size of 0.1-0.2 µm while fog droplets are an order of magnitude larger than haze particles and clear air defines the absence of particles (McCartney 1976). The laser range based solely on attenuation for these three atmospheric conditions is given in Table 7. The equation used to calculate these values is given as follows:

$$\tau(R) = \frac{P(R)}{P(0)} = e^{-\sigma R} \tag{25}$$

where τ is the transmittance, P is the laser power, R is the range, and σ is the attenuation coefficient (Weichel 1990). Plots showing the laser transmittance as a function of range for each atmospheric condition can be found in Appendix C. As can be seen the laser's range is very great even in fog. Due to laser's extensive range, the sound output from the acoustic-laser vibrometry system is the more limiting factor due to spherical spreading if a loudspeaker is used. Also listed in Table 7 is the approximate sound pressure level (SPL) needed 1 meter from the sound source to reach the maximum laser range. This accounts only for the sound pressure coming from the source and does not account for any interference from other potential sources.

It is not feasible to have a sound source that could produce such a high volume sound as it would have to be rather large and difficult to make portable. Additionally the high SPL required is at or above the range of what is considered safe exposure without hearing loss. While it would be possible for operators to wear proper hearing protection, it would be difficult to ensure all personnel in the range of the equipment have appropriate protection.
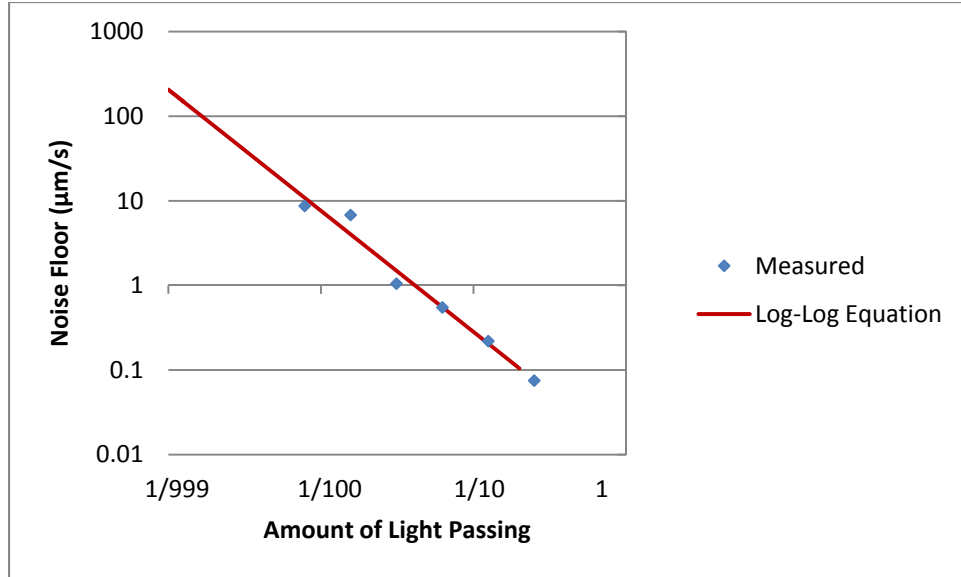

Figure 23: Noise floor level of response vs. Amount of light passing for a 2500 Hz tone

Table 7: Laser Range and Sound Pressure Level required to reach range for various atmospheric conditions

Condition	Max Laser Range [m]	SPL at 1 m from source to reach max laser range [dB re 20 μPa]
Clear Air	31,950	166.87
Haze	3195	146.87
Fog	319.5	126.87

The use of a parametric acoustic array (PAA) in measurements would reduce the issue of sound range due to its more focused sound beam. A PAA has two sources of sound; one source is high frequency which is generated directly from one or more high-frequency transducers; the other is low frequency which is generated from nonlinear effects in the volume of air in front of the transducer. A PAA source can provide a practical means to deliver the necessary level of acoustic power in air to the void underneath the FRP sheet while minimizing system size and

48

weight, and reducing the sound level imposed on personnel close to the source. To be able to detect the voids of small size between FRP and steel, the use of a PAA source exhibits potential advantages on this particular application, but one was not available to use for measurements during this research.

5.1.6   Defect Mapping

After all the parameters had been evaluated, a defect mapping was created. The sound used for excitation was a 10 second duration 0-20 kHz frequency sweep. This was chosen so that each mode of vibration could be mapped and compared with finite element results for an elliptic plate. The mapping required measuring the defect in a grid pattern with a sweep done at every point. To map the defect, each point measurement was evaluated and the maximum vibration velocity amplitude at the chosen frequency was found. These values were then plotted on the same grid pattern to create a contour or 3D plot (Figure 24). Additional 3D plots of the other modes of vibration determined from both experimental and finite element results are given in Appendix D. Of note, the experimental 3D plots only show the amplitude, not the directionality of the response so they will match the finite element mode shapes, but will show the shape as all positive. Points outside the bounds of the defect show very little amplitude while ones on the defect show quite large amplitude. Multiple frequencies were chosen and the first five modes of vibration were able to be realized from the mapping.
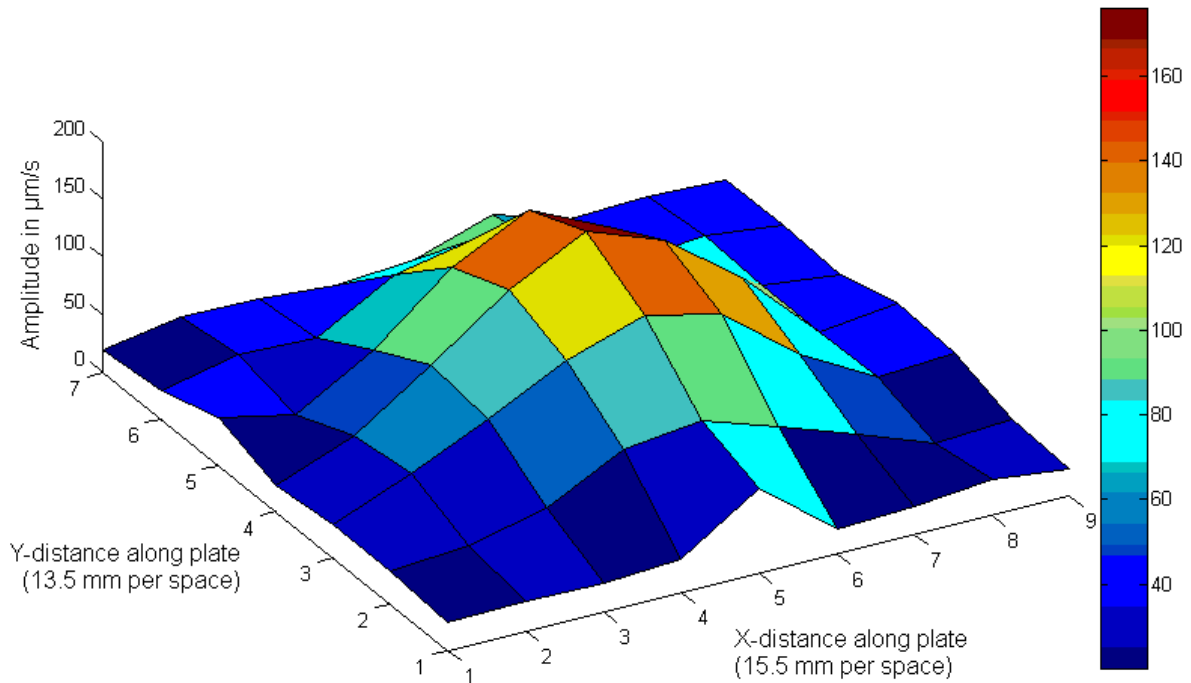
Figure 24: 3D surface plot mapping of specimen response in first mode of vibration (2550 Hz)

5.2 Comparison of Theoretical, Finite Element, and Measured Results

The measured vibration modes were compared with the finite element analysis and the theoretical solutions to elliptical plate vibrations. The results from theoretical, experimental, and numerical sources were compared to see the resemblance of both modal shape and frequency. Of note, the theoretical results required rounding the major axis to minor axis ratio to 1.2 (in reality it is 1.28). The finite element analysis was conducted with fixed boundary conditions and simply supported conditions to properly bound the possible frequencies. Table 8 shows the results of the finite element analysis, theoretical calculations, and experimental measurements for the first five modes of vibration and they are also plotted in Figure 25. The use of finite element analysis and analytical methods validated the acoustic laser method. The comparison of these results also shows that the proper model is of the plate above the defect is actually a plate with a boundary condition that is something between fixed and simply supported. Unfortunately there is not a certain way to model this so the error was not able to be corrected any further. However, the relative nearness of the results from different sources is promising for the laser acoustic NDT method. Also of interest is the actual measured results for the first mode are very close to

50

models with fixed boundary conditions, but by the time the fifth mode is reached, the actual

measurements more closely resemble simply supported boundary conditions.

Table 8: Comparison of theoretical, finite element, and measured frequencies of first five modes of vibration with percent error from measured

| Mode	LDV Measured	Theoretical (fixed)		Theoretical (simply supported)		FEA (fixed, 3D solid element)		FEA (fixed, shell element)		FEA (simply supported, shell element)	
	Frequency (Hz)	Frequency (Hz)	% Error	Frequency (Hz)	% Error	Frequency (Hz)	% Error	Frequency (Hz)	% Error	Frequency (Hz)	% Error
1	2515	2795	11%	1351	-46%	3044	21%	3036	21%	1448	-42%
2	4275	5272	23%	3748	-12%	5461	28%	5431	27%	3481	-19%
3	5380	6309	17%	4159	-23%	6878	28%	6855	27%	4592	-15%
4	6745	8716	29%	6371	-6%	8773	30%	8686	29%	6389	-5%
5	7580	9488	25%	6950	-8%	9891	30%	9840	30%	7304	-4%
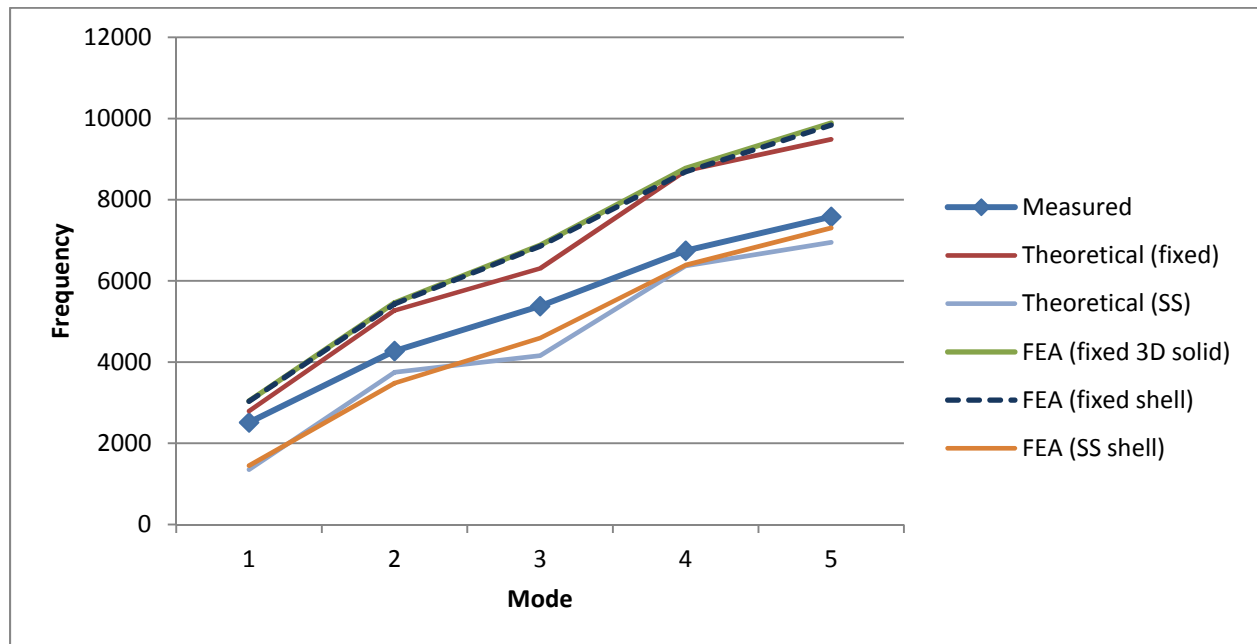
Figure 25: Graphic comparison of theoretical, finite element, and measured results for first five modes of vibration

5.3 Probability of Detection

For the purposes of this thesis, the probability of detection is referring to a comparison of the rate of true positive defect identification to the rate of false positive defect identification. The comparison of the true and false positive rates results in the receiver operating characteristics (ROC) graph. These were determined by using the data collected from one of the modal mappings discussed in Section 5.1.6. The ROC graph shows how the parameters set for a detection threshold will affect the false positive as compared to the true positive. The goal is to choose a point on the ROC curve that is as close as possible to the top left corner of the graph (Fawcett 2006). This would indicate a false positive rate of zero and a true positive rate of one or 100%, thereby detecting all the defects without detecting any false alarms. Figure 26 and Figure 27 shown below indicate the ROC curve and the true and false positive rates as a function of the detection threshold respectively. The ROC curve (Figure 26) can be used to pick the point that gives the best combination of true and false positive identification rates and then Figure 27 can be used to determine with those identification rates, what is the vibration velocity amplitude (in μm/s). In this case, the best possible scenario occurs when the vibration velocity equals 51 μm/s, where the false positive rate will be zero and the true positive rate will by .7593 or 75.9%. While this point is the closest to the top left corner, it does not fully capture all of the true positive defects. The point could be chosen to be further from the top left with the understanding that a larger false alarm rate could occur.
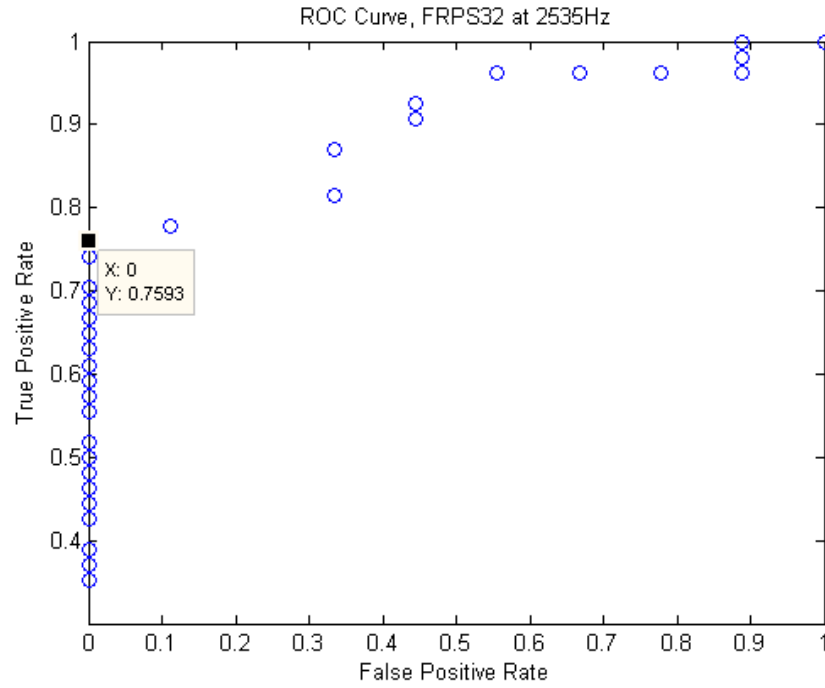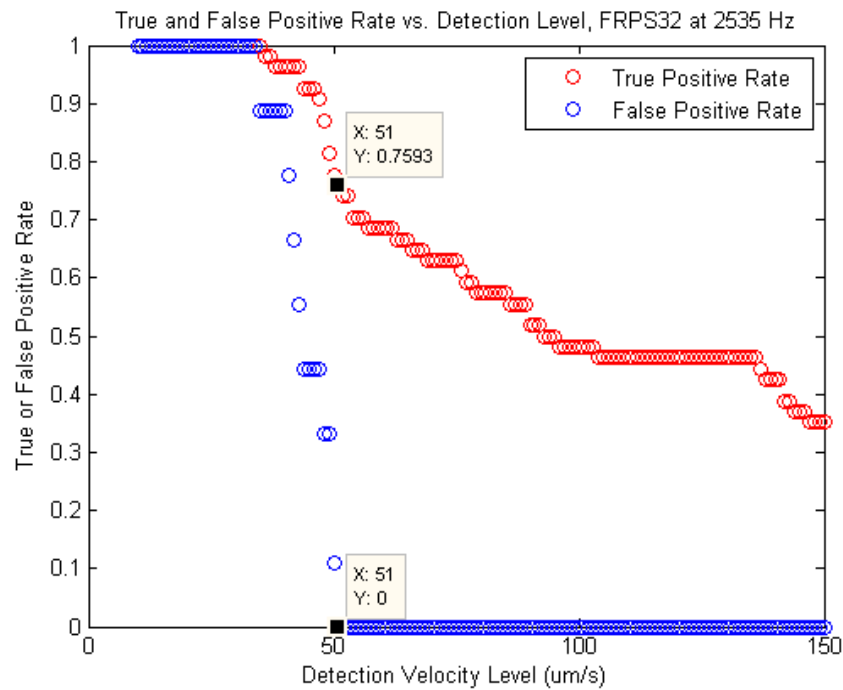
Figure 26: ROC Curve at 2535 Hz

Figure 27: True and False Positive Rates at 2535 Hz

5.4 On-site Acoustic LDV System Parameters

This analysis of detection probability leads into the establishment of specific parameters for an on-site system for measuring for these defects. Detection threshold defines the level of

vibration velocity (in μm/s) above which an area will be defined as a defect and below which is defined as intact. Based on the analysis from Section 5.3, the detection threshold for specimens similar to this one should be set to 51 μm/s. While this will not identify every defect in its entirety due to the true positive rate of only 75.9%, it will identify the defects that are of a size that is relevant to the structure. Additionally, based on the input data, the lower true positive rate means that a defect of this size will be detected, but the size will be assumed to be slightly smaller than it actually is. This is not an issue because anywhere a defect is detected will require a much more detailed and critical look than a simple passing sweep with the acoustic LDV equipment.

Another parameter that bears discussion is the frequency sweep range and time. All the frequency sweeps used in this research were from 0-20 kHz but such a large range may not be necessary. While it is highly dependent on the material properties of the structure to be tested and the size of defect that is determined to be relevant structurally, the frequency range may not need to go all the way to 20 kHz. It could easily be chosen to go only to 10 or 15 kHz which would give more detail to the range for the same time of sweep. In the case of the defect specimen used for these measurements, a sweep from 0-10 kHz would have easily covered the first 5 modes of vibration thereby being sufficient to fully identify the defect. Additionally, once the modes are beyond about the second or third mode they become increasingly more difficult to discern against the background noise. For frequency sweep time duration, a constantly repeated sweep of 0.1 s gave results of the same quality as a 60 s sweep. Therefore a 0.1 s sweep constantly repeated should be used for real world measurements. This way the sweep can be constantly played and the laser can be aimed from one spot to the next and 0.1 s measurements taken without having to worry about starting or stopping the sound that is playing. The ability to only have to worry about setting the laser while letting the sound play continuously will be crucial for productivity with the acoustic LDV system.

The sound pressure level output required at the speaker depends entirely on the range required for the structure being measured. A sound source capable of at least 100 dB should be used especially for close ranges (a few meters) but the requirement beyond that distance can grow exceedingly large. To get extended range out of the acoustic laser system, a sound source such as a PAA could be used.

The laser itself does not limit the range very much; the only issue is to ensure that the laser vibrometer chosen for the system has a good return (reflection) off the structure. For the purposes of this research retro-reflective tape was used as it discretized the area to be measured but also because it gave a better return off the structure. It would be highly unproductive to have to place this tape all over the structure to be measured prior to measuring it. A higher quality laser would likely be able to perform properly without the tape, but one was not available during the measurements conducted during this research.

The angle at which a given structure should be measured should not have an incident angle of less than 30 degrees. This is due to the increased noise and poor return once the angle gets below this for frequency sweeps. The best angle for NDT measurements with the acoustic LDV system is 90 degrees (perpendicular) to the structure being measured. However, this could present some issues for the underside of a bridge or the exterior hull of a ship that can only be accessed from one side or is anchored in a harbor away from a pier from which measurements could be taken. The sine squared functional relationship between angle and vibration amplitude must be accounted for to ensure accurate results and minimize the number of defects that are not found.

5.5 Measurement Methodology

The methodology by which a structure should be tested with the acoustic LDV method was developed through the course of this research. First, prior to any measurements being taken, the structure's properties and design should be well understood. Based on these, a theoretical approximation of the first modal frequency can be made. The theoretical approximation will be used to set the range of frequency sweep to use for the structure. Additionally, the size of defect that will be significant enough to weaken the structure should be determined, again to help set the proper frequency range.

Once the frequency range has been set, the repeating 0.1 s frequency sweep can be played continuously while the laser vibrometer is moved from point to point on the structure. Important places to look for issues are joint terminations where stress concentrations occur and any area where the steel-epoxy-FRP interface is under a particularly high amount of stress. As the laser is moved from point to point, an immediate readout of the frequency response will be shown to the operator. If any increased response is noticed, the operator can check that area in more detail. This could mean using a denser grid of measurement points around the suspected defect, or using

what appears to be the first mode of vibration to get a more detailed picture. Each measurement point will be fed into a grid so that a mapping of the structure can be created after the entire structure has been measured. This allows for a very easy to understand graphic display of where defective areas are located.

6 Conclusions/Recommendations for Future Work

6.1 Conclusions

As the use of composite materials continues to become more prevalent, the acoustic LDV method shows promise for use on both naval and civil structures. The robustness of this method and its ability to be used at a standoff distance from the structure are great benefits. This research has proven that the acoustic laser method can be used to effectively identify delamination/debonding defects in the FRP-steel interface and can determine the size and nature of these defects as well. There is significant potential for the application of this technology to any structure incorporating FRP composite materials in conjunction with metals. The measurements that were taken with the acoustic LDV correlated with results determined through both theoretical and finite element analyses, thereby making it possible to use models of damage detection prior to actual measurements being taken. This will allow for better determination of the appropriate frequencies and sound power levels to use when taking measurements on a structure.

6.2 Recommendations for Future Work

There are several areas of the acoustic LDV method that require additional research. The first is to use higher quality equipment to help provide a better fidelity system. A sound source such as a PAA would allow for a much greater range and better focusing of the sound on the area to be investigated. Additionally, a higher quality laser would be able to have a return off of the material of the structure rather than requiring the addition of retro-reflective tape. Both of these items would be another step towards developing a system for employment in real world scenarios.

Furthermore, a more accurate representation of real world structures could be investigated. In this research only flat plates were joined and measured with the acoustic LDV method. This proved the concept is feasible, but there are numerous ways in which metal and

FRP materials can be joined. The complexity of the joint could have an impact on how the acoustic LDV system needs to be employed. This could be investigated through both experimental and finite element methods.

Another item requiring further work is realizing crack defects with the acoustic laser system. Part of the difficulty is inducing a crack in the specimen that would be realistic to what could be seen in a typical FRP-metal structural system. It is difficult to simply crack a specimen while leaving the rest of it intact. Also, while full through thickness cracks do seem promising to be identified by the acoustic laser system based on finite element analysis, it is also likely that these types of defects could be found visually without any form of NDT. This would limit acoustic LDV to only being used to detect cracks from a large distance where they could not be seen visually which would not be promising for this method. Additional work to better realize the partially cracked defect or to somehow increase the measured response level is necessary.

Further work could also be done to better define the boundary condition at the edge of the defect. In this research the boundary was modeled as both simply supported and fixed but neither gave perfect correlation. It is interesting that at low modes of vibration the response matches fixed boundary conditions but at higher modes it matches simply supported boundary conditions. No explanation was determined for this in the course of this research. However, more detailed analysis of this specific area with the aid of high powered microscopes or other types of finite element and molecular dynamics simulation could aid in identifying the causes of this phenomenon.

Appendix A – Vibration Velocity Response for Various Sweep Lengths
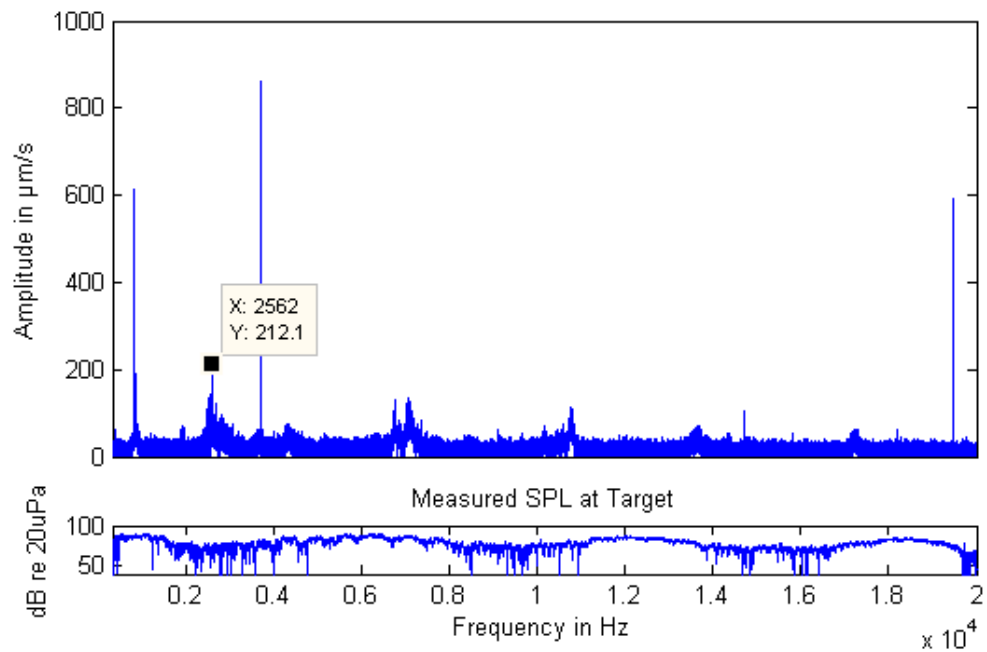
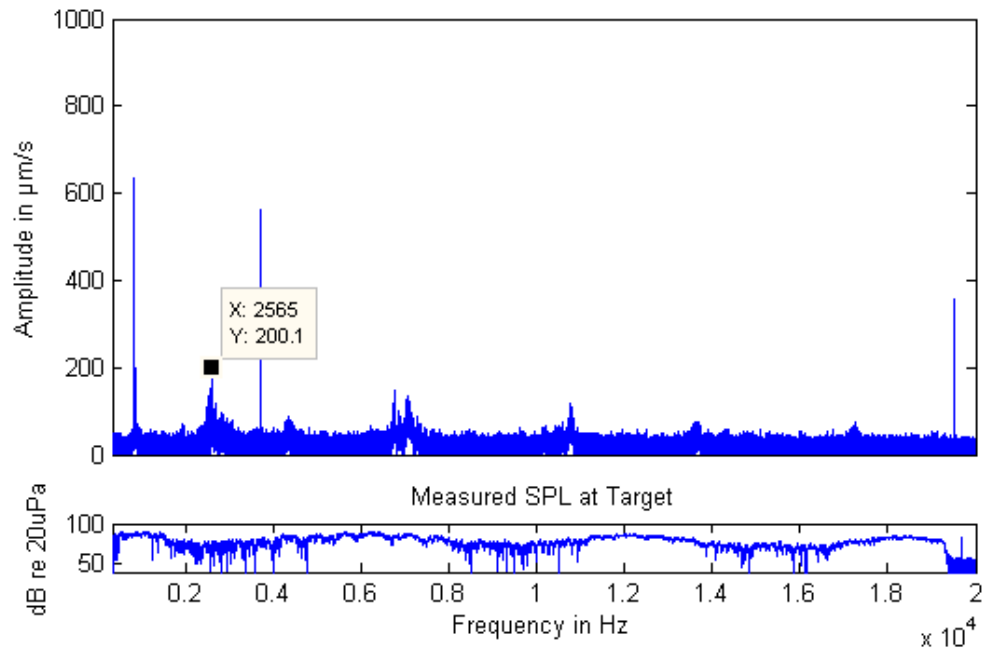**Figure A1: Frequency response plot for 60 s duration 0-20 kHz sweep**

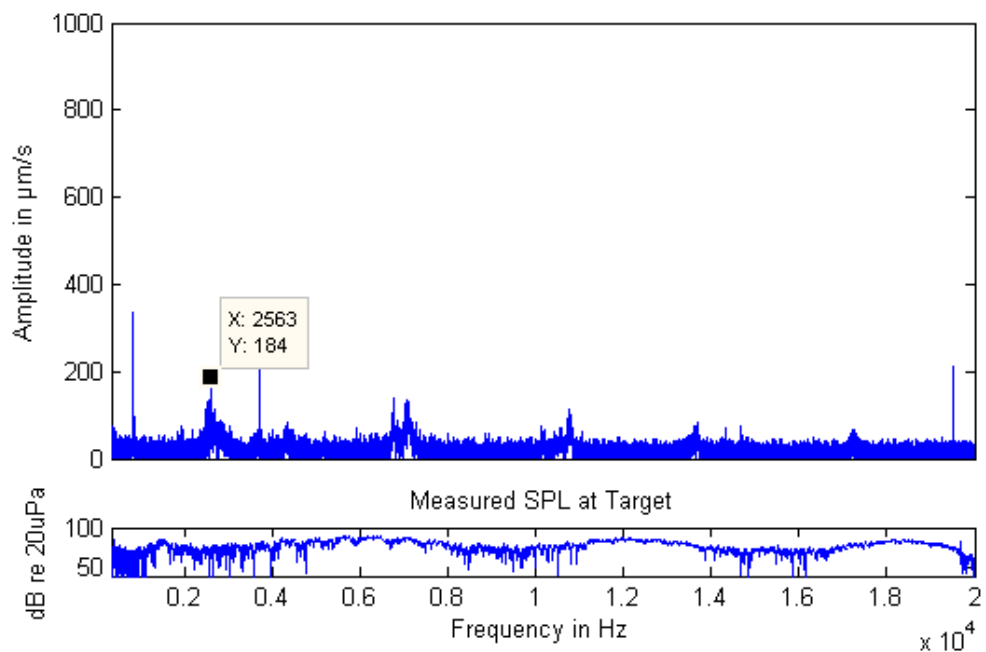**Figure A2: Frequency response plot for 10 s duration 0-20 kHz sweep**

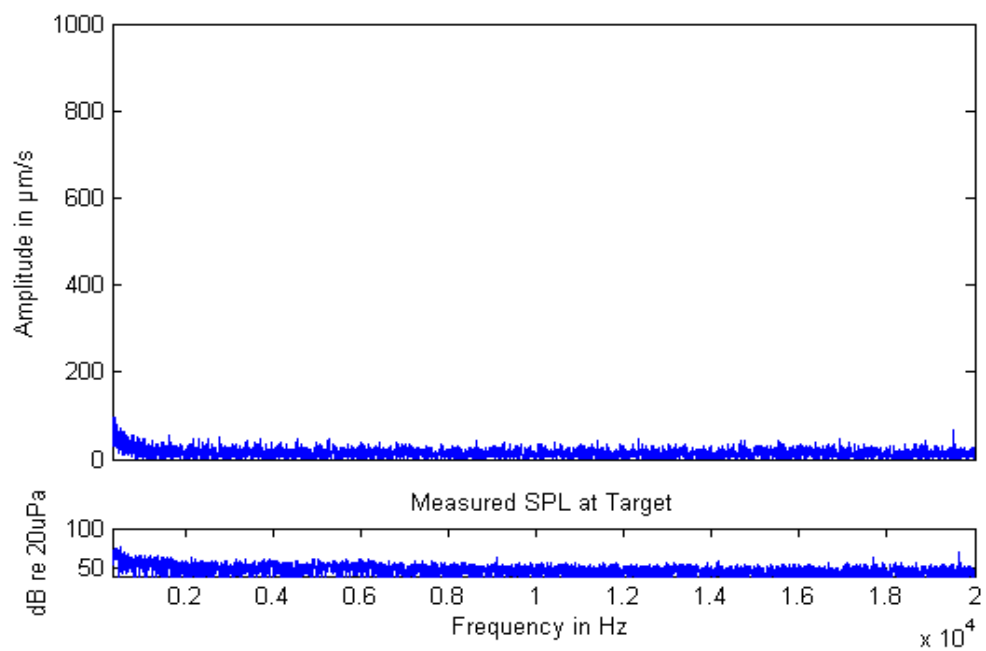**Figure A3: Frequency response plot for 1 s duration 0-20 kHz sweep**

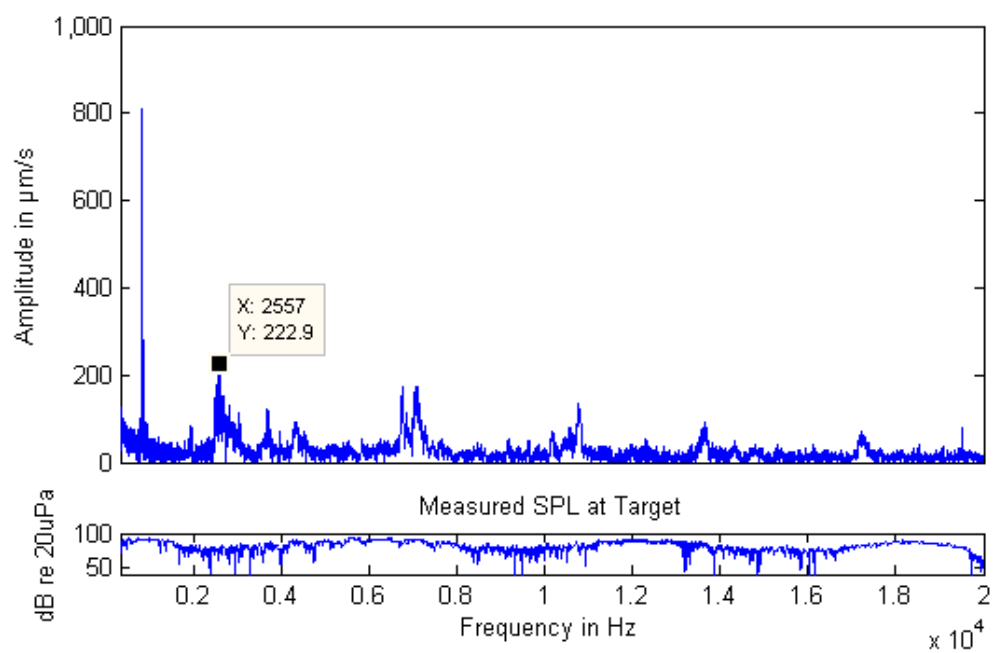**Figure A4: Frequency response plot for 0.1 s duration 0-20 kHz sweep**

Figure A5: Frequency response plot for 0.1 s duration 0-20 kHz sweep repeated continuously

Appendix B – Vibration Velocity Response for Various White Noise Times
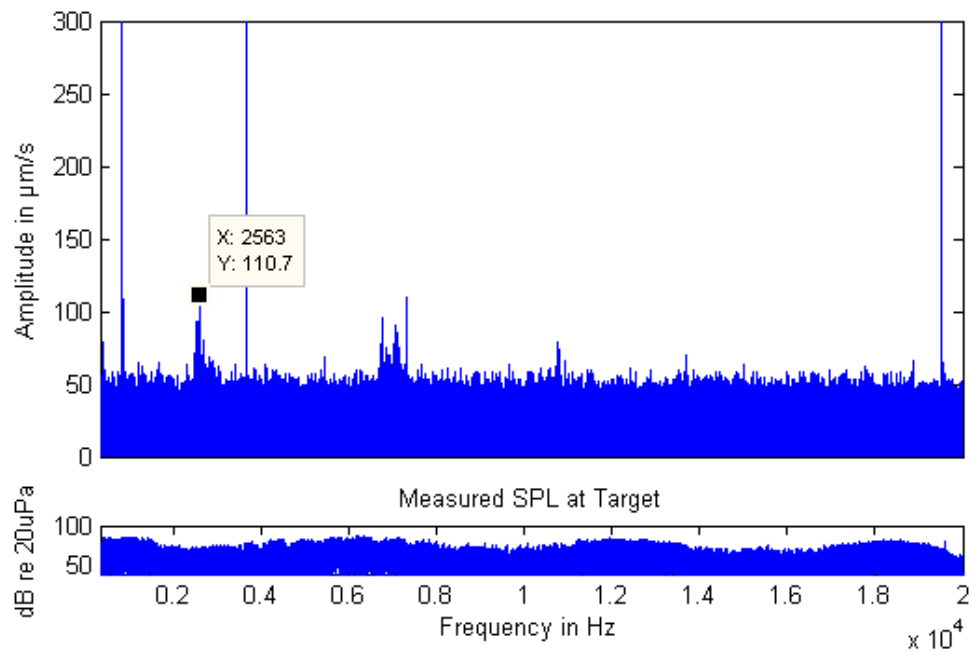
Figure B1: Frequency response plot for 60 s duration white noise
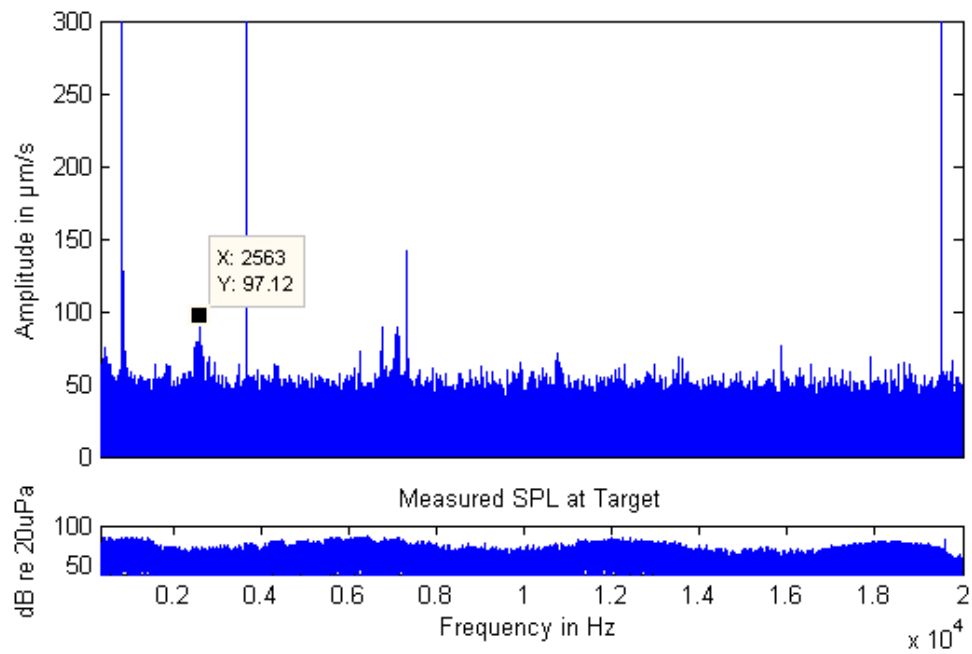
Figure B2: Frequency response plot for 10 s duration white noise
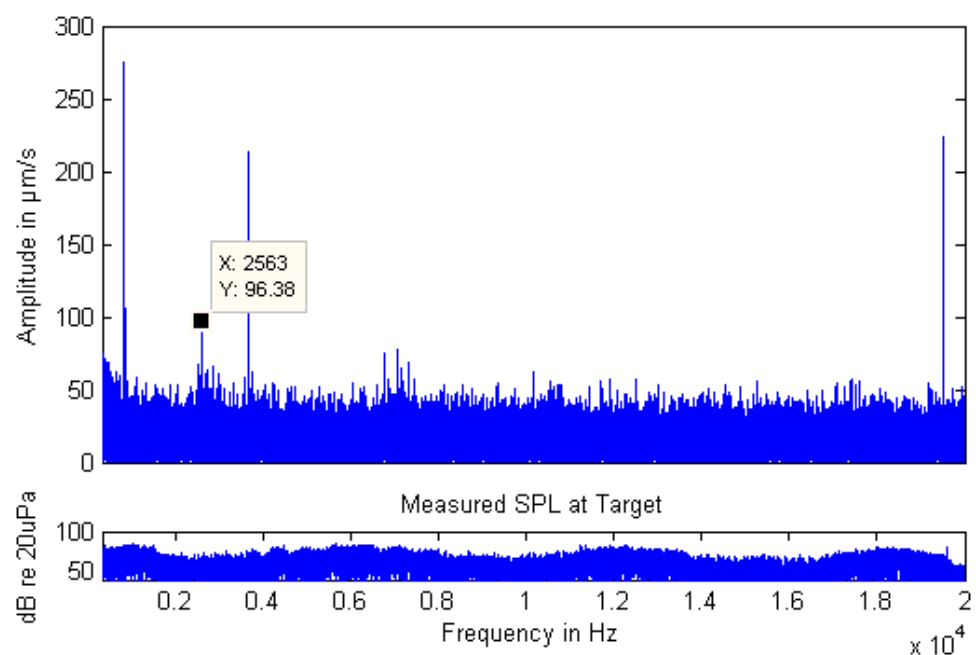
Figure B3: Frequency response plot for 1 s duration white noise
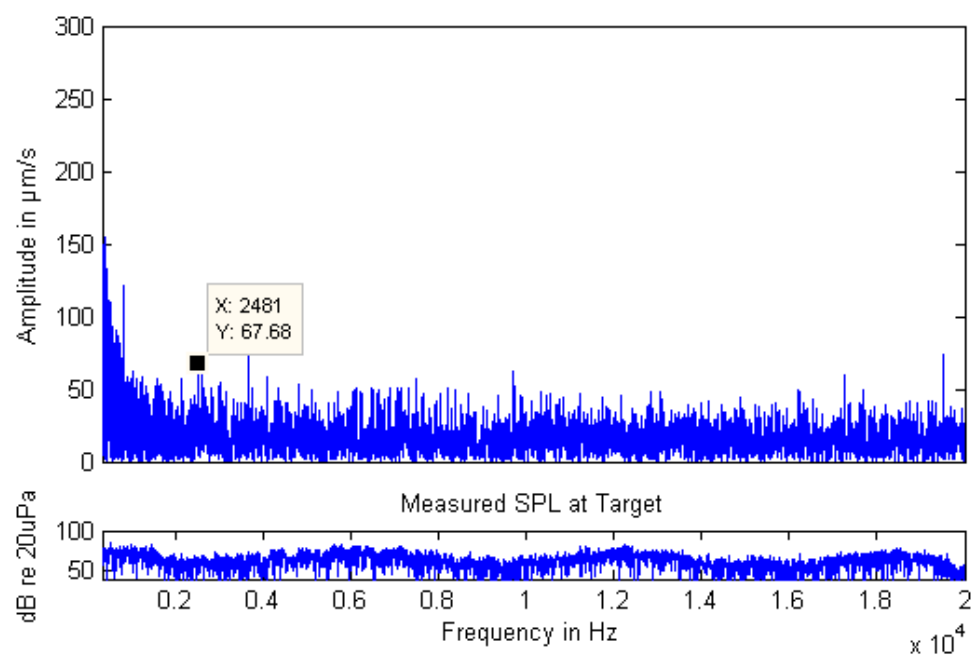
Figure B4: Frequency response plot for 0.1 s duration white noise

Appendix C – Transmittance vs. Range for Various Atmospheric Conditions
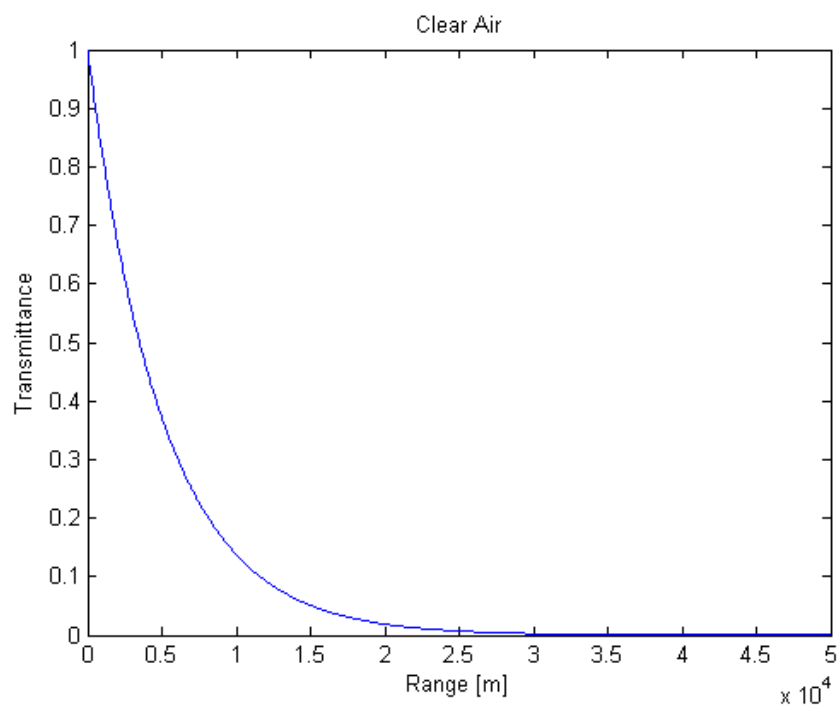
Figure C1: Clear air transmittance vs. range
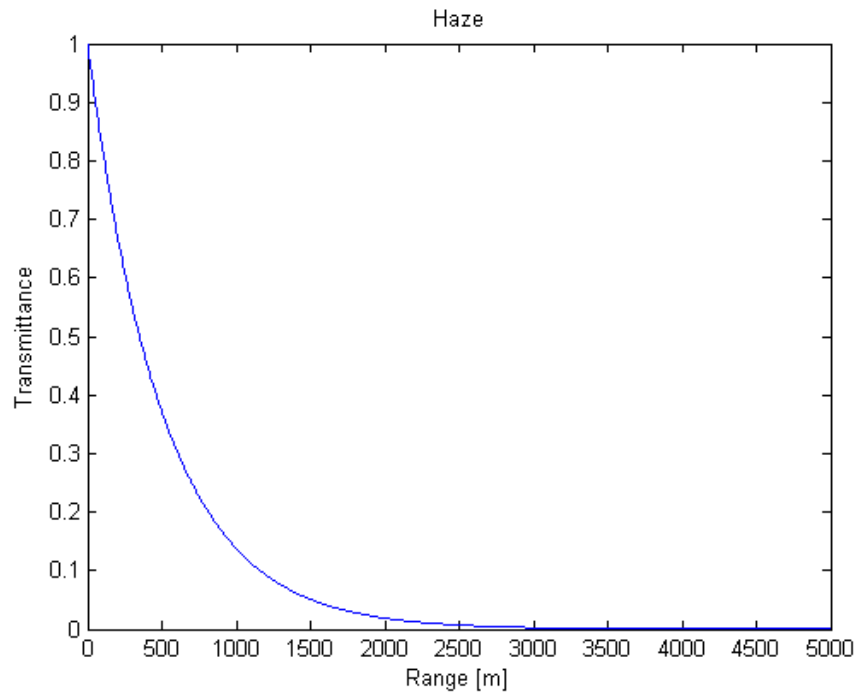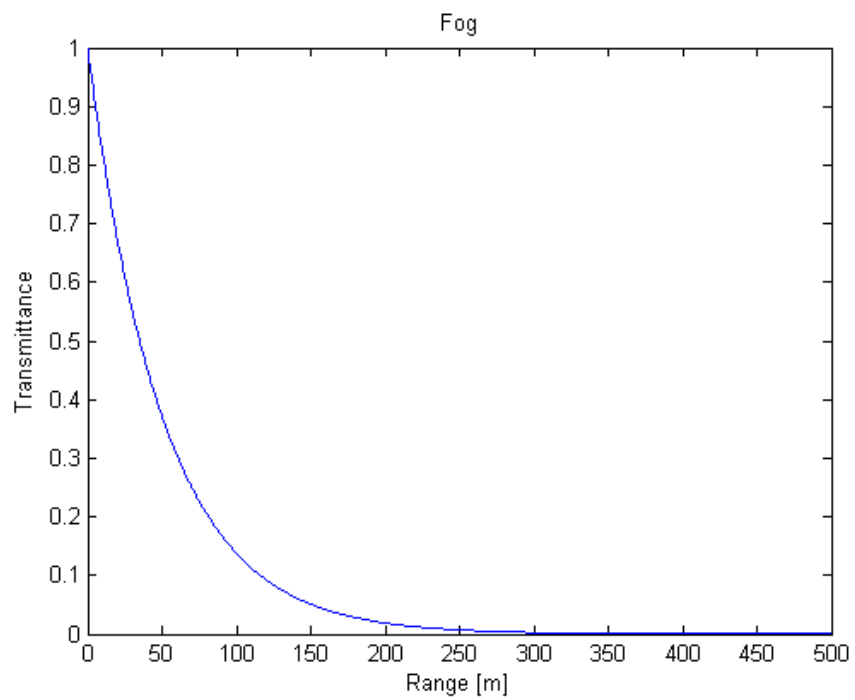

Figure C2: Haze transmittance vs. range

Figure C3: Fog transmittance vs. range

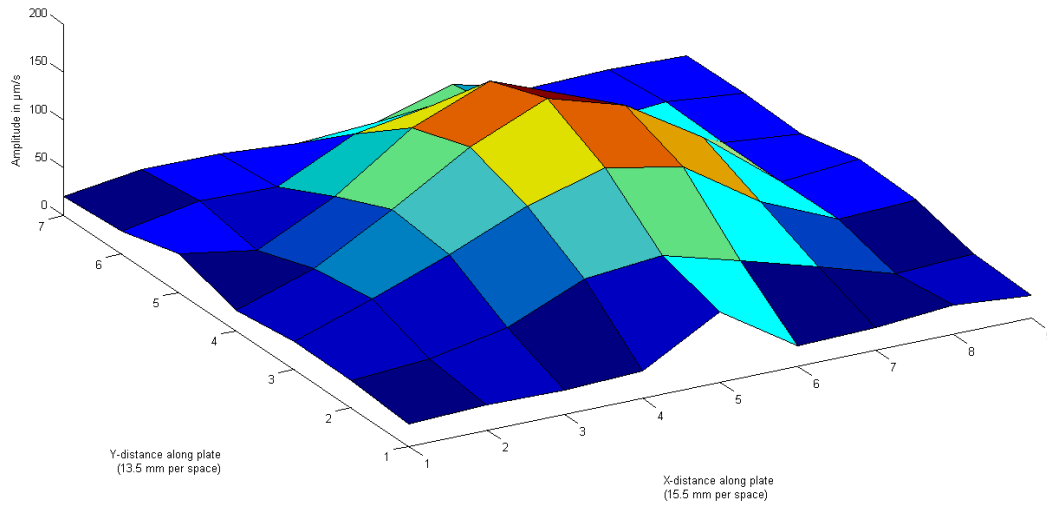# Appendix D – Comparison of Measured Modal Response to Numerical Results

Figure D1: 3D surface plot mapping of specimen response in first mode of vibration (2535 Hz)
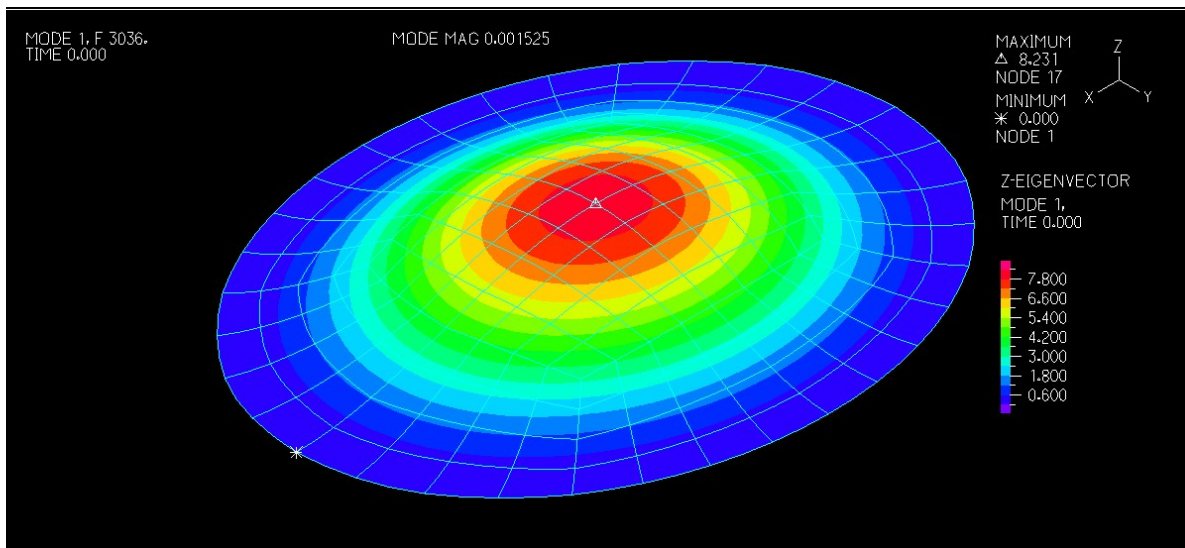

Figure D2: Finite element analysis representation of first vibration mode (notional to show mode shape, units negligible)
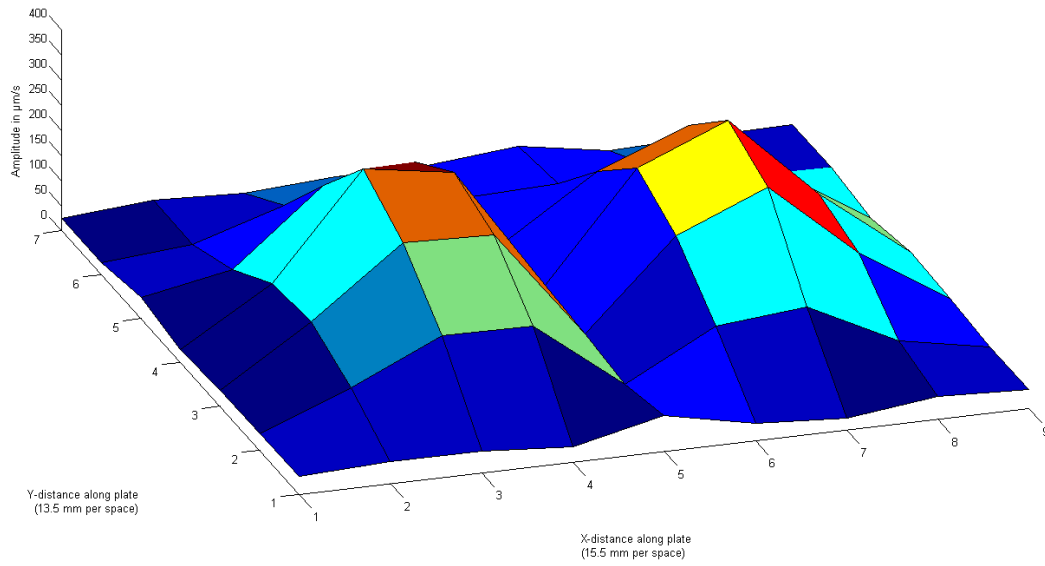
Figure D3: 3D surface plot mapping of specimen response in second mode of vibration (4275 Hz)
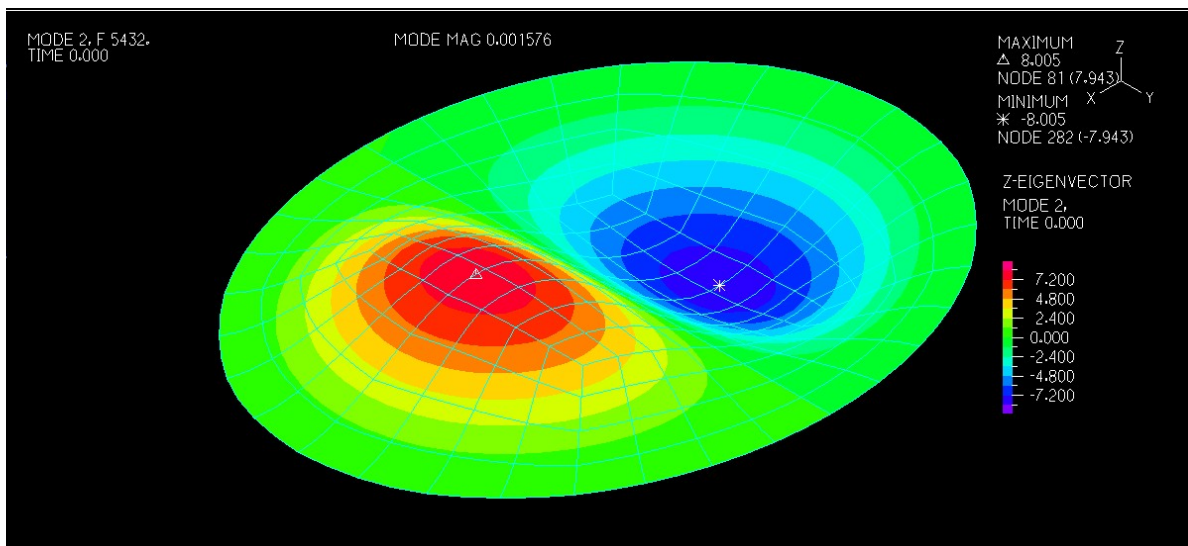

Figure D4: Finite element analysis representation of second vibration mode (notional to show mode shape, units negligible)
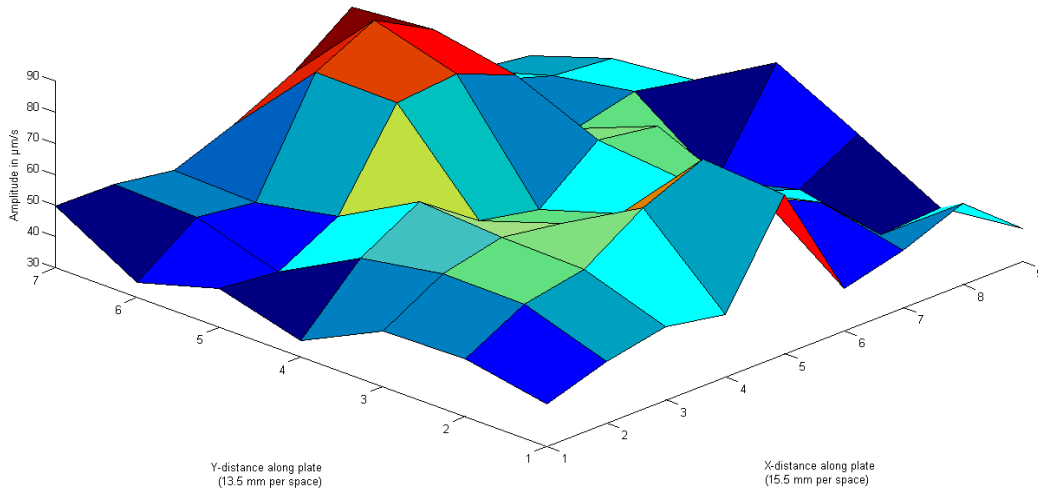
66

Figure D5: 3D surface plot mapping of specimen response in third mode of vibration (5380 Hz)

Figure D6: Finite element analysis representation of third vibration mode (notional to show mode shape, units negligible)

67

Figure D7: 3D surface plot mapping of specimen response in fourth mode of vibration (6745 Hz)

Figure D8: Finite element analysis representation of fourth vibration mode (notional to show mode shape, units negligible)

Figure D9: 3D surface plot mapping of specimen response in fifth mode of vibration (7580 Hz)
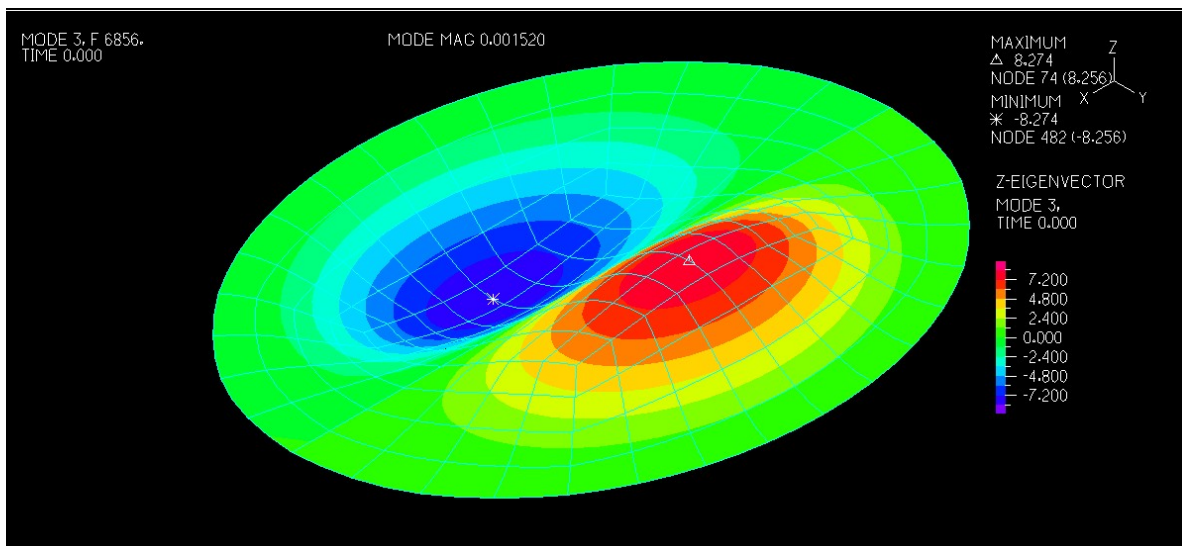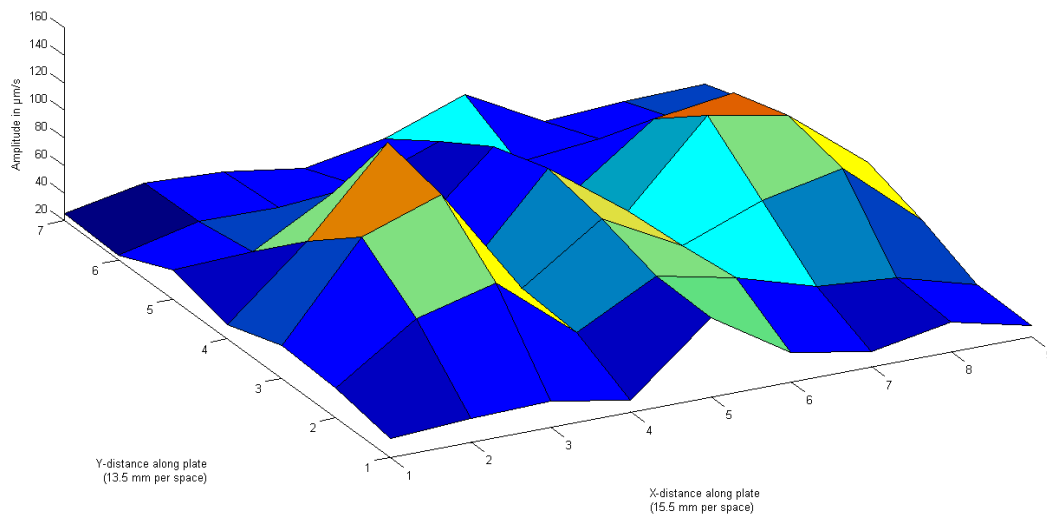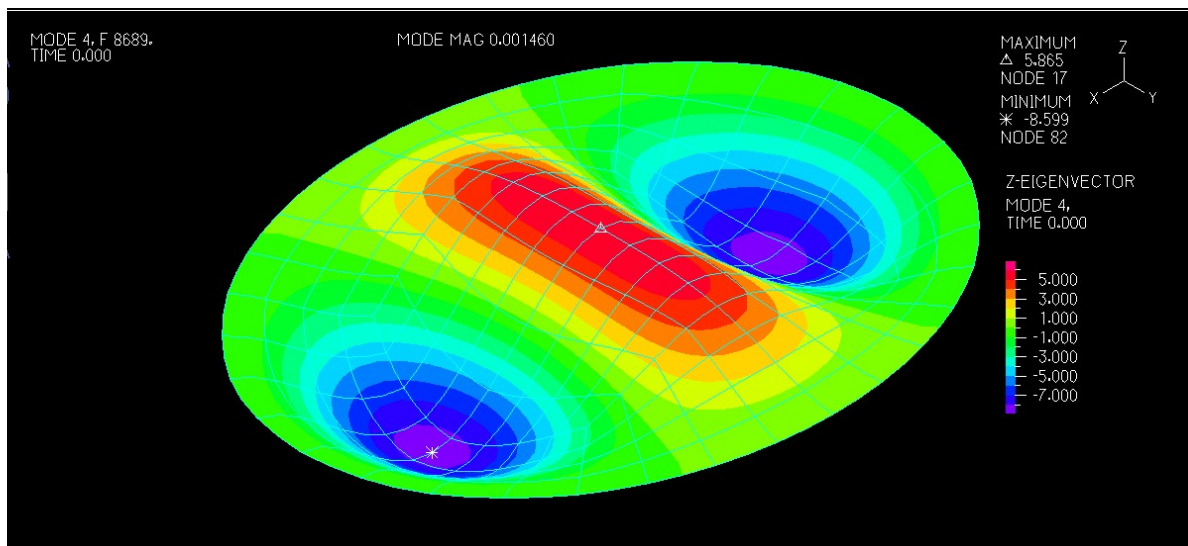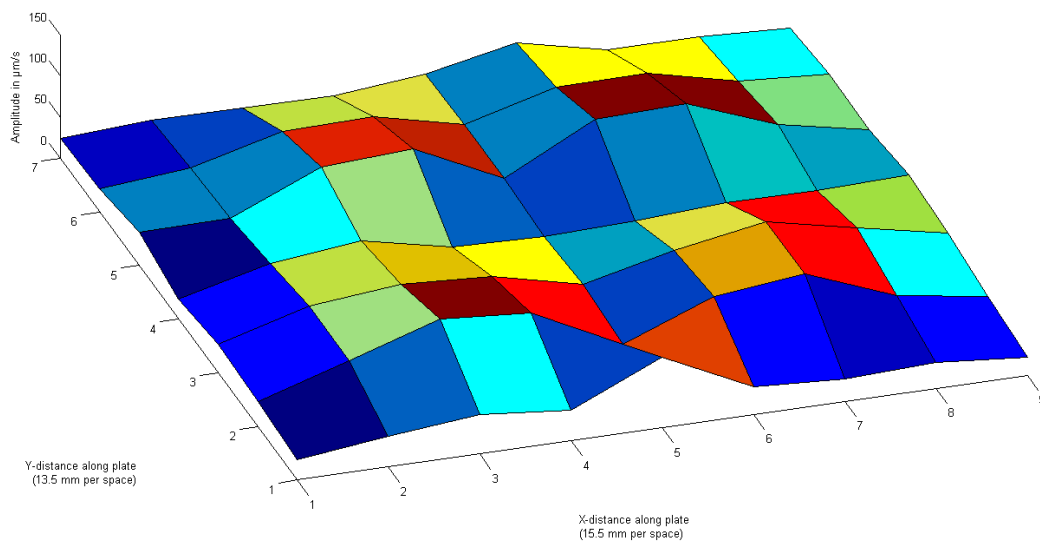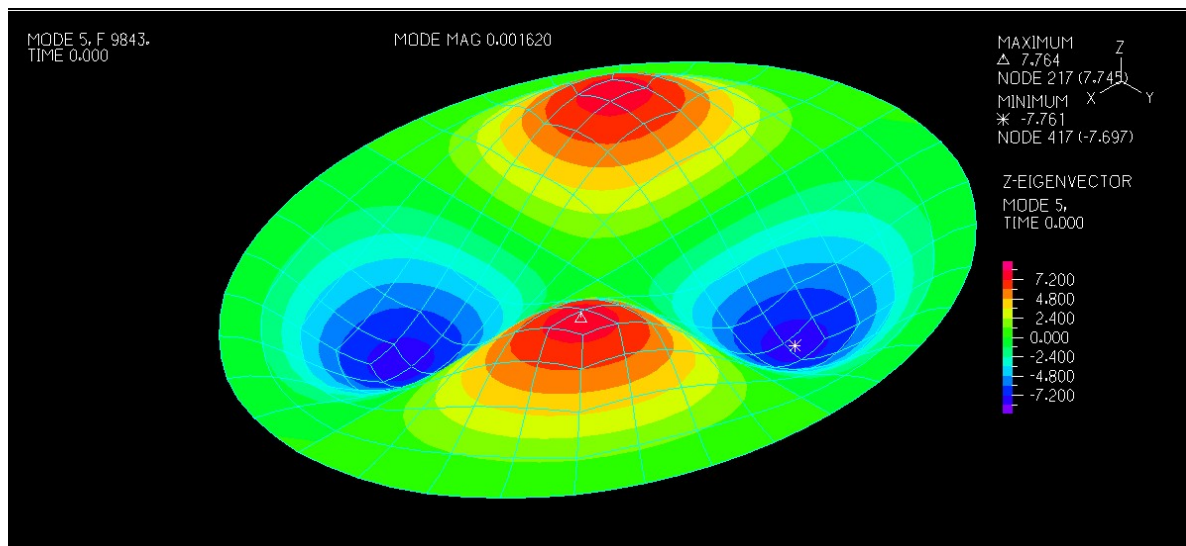

Figure D10: Finite element analysis representation of fifth vibration mode (notional to show mode shape, units negligible)

69

References

ADINA R & D, Inc. "Theory and Modeling Guide." Watertown, MA: ADINA R & D, Inc., 2011.

Amraoui, M. Y., and A. J. Lieven. "Laser vibrometry based on detection of delamination in glass/epoxy composites." *Transactions of SNAME* 126 (July 2004): 430-437.

Barsoum, R. G. S. "The Best of Both Worlds: Hybrid Ship Hulls Use Composites & Steel." *AMPTIAC Quarterly* (Advanced Materials and Processes Technology Information Analysis Center (AMPTIAC)) 7, no. 3 (2003): 55-61.

Bathe, K. J. "Finite Element Procedures." 200. USA: Klaus-Jurgen Bathe, 2006.

Buyukozturk, O., and H. C. Rhim. "Electromagnetic properties of concrete at microwave frequency range." *ACI Materials Journal* 95, no. 3 (1998): 262-271.

Buyukozturk, O., and T. Y. Yu. "A far-field airborne radar NDT technique for detecting debonding in GFRP-retrofitted concrete structures." *NDT & E International* 41, no. 1 (January 2008): 10-24.

Buyukozturk, O., O. Gunes, and K. Erdem. "Progress on understanding debonding problems in reinforced concrete and steel members strengthened using FRP composites." *Construction and Building Materials* 18 (2004): 9-19.

Buyukozturk, O., R. Haupt, C. Tuakta, and J. Chen. "Remote Detection of Debonding in FRP-Stengthened Concrete Structures using Acoustic-Laser Technique." In *Nondestructive Testing of Materials and Structures*, by O. Buyukozturk and M. A. Tasdemir. Springer, 2011.

Camponeschi, E. T., R. Crane, K. Lipetzky, and B. Bandos. "The Role and Use of Nondestructive Testing for US Navy Composite Ship Structures." *Materials Evaluation* 65, no. 7 (July 2007): 752-758.

Castellini, P., E. Esposito, N. Paone, and Tomasini. "Non-invasive measurements of damage of frescoes painting and icon by Laser Scanning Vibrometer: experimental results on artificial samples and real works of art." *Proceedings of SPIE* 3411 (1998): 439-448.

Clemena, G. G. "Short-pulse radar methods." In *Handbook on Nondestructive Testing of Concrete*, by V. M. Malhotra and Nicholas J. Carino, 253-274. CRC Press, 1991.

DDG-1000 Zumwalt Class - Multimission Destroyer, United States of America. 2011. http://www.naval-technology.com/projects/dd21/dd216.html (accessed November 9, 2011).

De Andrade, R. M., E. Esposito, N. Paone, and G. M. Revel. "Non-destructive techniques for detection of delamination in ceramic tile: a laboratory comparison between IR thermal camerals and laser Doppler vibrometers." *Proceedings of SPIE* 3585 (1999): 367-377.

Drain, L. E. *The Laser Doppler Technique.* Chichester, NY: John Wiley & Sons, 1980.

Farmer, N., and Ian Smith. "King Street Railway Bridge - Strengthening of Cast Iron Girders with FRP Composites." *9th International Conference and Exhibition on Structural Faults and Repair.* London, UK: Engineering Technics Press, 2001.

Fawcett, T. "An introduction to ROC analysis." *Pattern Recognition Letters* 27 (2006): 861-874.

Fenning, P. J., and A. J. Brown. "Ground Penetrating Radar Investigation." *Construction Repair* 9, no. 6 (1995): 17-21.

Ghoshal, A., A. Chattopadhyay, M. J. Schulz, R. Thornburgh, and K. Waldron. "Experimental investigation in composite material structures using a laser vibrometer and piezoelectric actuators." *Journal of Intelligent Material Systems and Structures* 14 (2003): 521-537.

Hollaway, L. C., and J. Cadei. "Progress in the technique of upgrading metallic structures with advanced polymer composites." *Progress in Structural Engineering and Materials* 4 (2002): 131-148.

Kim, I. I., B. McArthur, and E. Korevaar. "Comparison of laser beam propagation at 785 nm and 1550 nm in fog and haze for optical wireless communications." *Optical Wireless Communcations III.* SPIE, 2001. 26-37.

Krishnapillai, M., R. Jones, I. H. Marshall, M. Bannister, and N. Rajic. "Thermography as a tool for damage assessment." *Composite Structures* 67 (2005): 149-155.

LeGault, M. R. "DDG-1000 Zumwalt: Stealth warship." *Composites World.* February 2010. http://www.compositesworld.com/articles/ddg-1000-zumwalt-stealth-warship (accessed December 16, 2011).

Leissa, A. W. *Vibration of Plates.* Washington, D.C.: Scientific and Technical Information Division, National Aeronautics and Space Administration, 1969.

Levin, R. I., N. A. J. Lieven, and G. W. Skingle. "Comparison of accelerometer and laser Doppler vibrometer measurement techniques." *Proceedings of SPIE* 3411 (1998): 502-513.

Liang, Y., C. Sun, and F. Ansari. "Acoustic emission characterization of damage in hybrid fiber reinforced polymer rods." *Journal of Composites for Construction* 8, no. 1 (2004): 70-78.

Luke, S. "The use of carbon fibre plates for the strengthening of two metallic bridges of an historic nature in the UK." *FRP Composites in Civil Engineering.* Hong Kong, China: Elsevier Science Ltd., 2001. 975-983.

McCartney, E. J. *Optics of the Atmosphere.* New York: J. Wiley & Sons, 1976.

McNitt, R. P. "Free Vibration of a Damped Elliptical Plate." *Journal of Aerospace Sciences*, September 1962: 1124-1125.

Mellet, J. S. "Ground penetrating radar applications in engineering, environmental management, and geology." *Journal of Applied Geophysics* 33 (1995): 157-166.

Miller, T. C., M. J. Chajes, D. R. Mertz, and J. N. Hastings. "Strengthening of a Steel Bridge Girder Using CFRP Plates." *Journal of Bridge Engineering*, November/December 2001: 514-522.

Nagem, R. J., J. M. Seng, and J. H. Williams. "Residual Life Predictions of Composite Aircraft Structures via Nondestructive Testing, Part 1: Prediction Methodology and Nondestructive Testing." *Materials Evaluation* 58, no. 9 (2000): 1065-1074.

NavSource Naval History: Photographic History of the U.S. Navy. August 14, 2009. http://www.navsource.org/archives/10/09/10092123.jpg (accessed November 9, 2011).

Rajalingham, C., and R. B. Bhat. "Vibration of elliptic plates using characteristic orthogonal polynomials in the Rayleigh-Ritz method." *International Journal of Mechanical Sciences* 33, no. 9 (1991): 705-716.

Rajalingham, C., R.B. Bhat, and G.D. Xistris. "A note on elliptical plate vibration modes as a bifurcation from circular plate modes." *International Journal of Mechanical Sciences* 37, no. 1 (1995): 61-75.

Shibaoka, Y. "On the Transverse Vibration of an Elliptic Plate with Clamped Edge." *Journal of the Physical Society of Japan* 11, no. 7 (July 1956): 797-803.

Simler, J., and L. Brown. "21st Century Surface Combatants Require Improved Composite-to-Steel Adhesive Bonds." *AMPTIAC Quarterly* (Advanced Materials and Processes Technology Information Analysis Center (AMPTIAC)) 7, no. 3 (2003): 21-25.

Stanbridge, A. B., and D. J. Ewins. "Measurement of translational and angular vibration using a scanning laser Doppler vibrometer." *Shock and Vibration* 3, no. 2 (1996): 141-152.

Summers, C. *Stealth ships steam ahead.* June 10, 2004. http://news.bbc.co.uk/2/hi/technology/3724219.stm (accessed December 16, 2011).

Timoshenko, S., D. H. Young, and W. Weaver Jr. *Vibration Problems in Engineering.* Fourth Edition. New York: John Wiley & Sons, 1974.

Vanlanduit, S., P. Guillaume, and J. Schoukens. "Broadband vibration measurements using a continuously scanning laser vibrometer." *Measurement Science and Technology* 13 (2002): 1574-1582.

Visby Class Corvette. June 30, 2008.
http://en.wikipedia.org/wiki/File:K32_HMS_Helsingborg_Anchored-of-Gotska-
Sandoen_cropped.jpg (accessed November 9, 2011).

Visby Class, Sweden. 2011. http://www.naval-technology.com/projects/visby/ (accessed
December 16, 2011).

Wang, X., and V. Gupta. "Construction and characterization of chemically joined stainless
steel/E-glass composite sections." *Mechanics of Materials* 37 (2005): 1198-1209.

Weichel, H. *Laser Beam Propagation in the Atmosphere.* Bellingham, WA: SPIE Optical
Engineering Press, 1990.

Williams, J. H. "Stresses in Adhesive between Dissimilar Adherends." *Journal of Adhesion* 7
(1975): 97-107.

Williams, J. H., and R. J. Nagem. "A Liquid Crystals Kit for Structural Integrity Assessment of
Fiberglass Watercraft." *Materials Evaluation* 41 (February 1983).

Williemann, D. P., P. Castellini, G. M. Revel, and E. P. Tomasini. "Structural damage
assessment in composite material using laser Doppler vibrometry." *Proceedings of SPIE* 5503
(2004): 375-379.

Zhao, X. L., and L. Zhang. "State-of-the-art review on FRP strengthened steel structures."
Engineering Structures 29 (2007): 1808-1823.